

## Imprints of the Local Bubble and Dust Complexity on Polarized Dust Emission

GEORGE HALAL <sup>1,2</sup>, S. E. CLARK <sup>1,2</sup> AND MEHRNOOSH TAHANI <sup>1,2,3</sup>

<sup>1</sup>*Department of Physics, Stanford University, Stanford, CA 94305, USA*

<sup>2</sup>*Kavli Institute for Particle Astrophysics and Cosmology, Stanford, CA 94305, USA*

<sup>3</sup>*Banting and KIPAC Fellow, Stanford, CA 94305, USA*

### ABSTRACT

Using 3D dust maps and Planck polarized dust emission data, we investigate the influence of the 3D geometry of the nearby interstellar medium (ISM) on the statistics of the dust polarization on large (80′) scales. We test recent models that assume that the magnetic field probed by the polarized dust emission is preferentially tangential to the Local Bubble wall, but we do not find an imprint of the Local Bubble geometry on the dust polarization fraction. We also test the hypothesis that the complexity of the 3D dust distribution drives some of the measured variation of the dust polarization fraction. We compare sightlines with similar total column densities and find that, on average, the dust polarization fraction decreases when the dust column is substantially distributed among multiple components at different distances. Conversely, the dust polarization fraction is higher for sightlines where the dust is more concentrated in 3D space. This finding is statistically significant for the dust within 1.25 kpc, but the effect disappears if we only consider dust within 270 pc. In conclusion, we find that the extended 3D dust distribution, rather than solely the dust associated with the Local Bubble, plays a role in determining the observed dust polarization fraction at 80′. This conclusion is consistent with a simple analytical prediction and remains robust under various modifications to the analysis. These results illuminate the relationship between the 3D geometry of the ISM and tracers of the interstellar magnetic field. We discuss implications for our understanding of the polarized dust foreground to the cosmic microwave background.

*Keywords:* Interstellar dust (836) — Cosmic microwave background radiation (322) — Algorithms (1883) — Interstellar magnetic fields (845) — Interstellar medium (847) — Galaxy magnetic fields (604) — Milky Way magnetic fields (1057) — Magnetic fields (994) — Superbubbles (1656) — Interstellar reddening (853) — Interstellar dust extinction (837) — Extinction (505)

### 1. INTRODUCTION

Interstellar magnetic fields play an important role in various astrophysical processes (see, e.g., Ferrière 2001; Heiles & Haverkorn 2012; Pattle et al. 2023). However, little is known about the magnetic field structure in the nearby interstellar medium (ISM). Some works have suggested connections between the local magnetic field structure and other tracers of ISM morphology, perhaps due to dynamical influences, e.g. the formation of struc-

tures like superbubbles (e.g., Santos et al. 2011; Frisch et al. 2012; Berdyugin et al. 2014; Tahani et al. 2022a,b).

Aspherical dust grains in the ISM emit photons with an electric field oriented preferentially along their long axes (Purcell 1975). The short axes of typical dust grains are preferentially aligned with the local magnetic field orientation (Andersson et al. 2015). As a result, their thermal emission is partially polarized perpendicular to the orientation of the magnetic field. Therefore, measurements of the polarized dust emission are used as a probe for the plane-of-sky magnetic field orientation in dusty regions of the ISM.

Recent evidence suggests that variations in the fractional polarization of the dust emission, i.e., the ratio of the polarized to the total intensity of the dust emis-

sion, over large angular scales in the diffuse sky are mainly driven by the structure of the magnetic field. Henceforth, we will refer to the fractional polarization of the dust emission as the dust polarization fraction. [Planck Collaboration et al. \(2020a\)](#) probed the influence of the magnetic field geometry on the dust polarization fraction by comparing the local polarization angle dispersion with the 353 GHz polarization fraction. They calculated the polarization angle dispersion for an annulus with inner and outer radii of 40' and 120', and found that the 353 GHz polarization fraction is anti-correlated with the local polarization angle dispersion at 160' resolution. They showed that this relationship is consistent with models that only include topological effects of the turbulent magnetic field, but otherwise have uniform dust properties and alignment. [Planck Collaboration et al. \(2020a\)](#) conclude that the dust polarization fraction and the dispersion of polarization angles are similarly sensitive to the structure of the magnetic field. [Hensley et al. \(2019\)](#) further showed that some of the variability in the dispersion of polarization angles, and thus the dust polarization fraction, can be explained by the magnetic inclination angle, i.e., the angle between the magnetic field and the plane of the sky. The dust polarization fraction is maximized when the magnetic field is tangential to the plane of the sky and zero when it is parallel to the line of sight. [Chen et al. \(2019\)](#) and [Sullivan et al. \(2021\)](#) used statistical properties of the observed dust polarization fraction to estimate the average inclination angle of molecular cloud-scale magnetic fields.

The observed dust polarization fraction also depends on other factors, such as the dust grain alignment efficiency ([King et al. 2019](#); [Medan & Andersson 2019](#)), the phase distribution of the neutral interstellar medium ([Lei & Clark 2023](#)), and measurement noise. However, the 3D structure of the magnetic field is one of the major factors ([Clark 2018](#); [Hensley et al. 2019](#); [Planck Collaboration et al. 2020a](#)).

Our Sun's current location is near the center of a superbubble, which is thought to have been created by supernova explosions within the past  $10\text{-}15 \times 10^6$  years ([Cox & Reynolds 1987](#); [Maíz-Apellániz 2001](#); [Breitschwerdt et al. 2016](#); [Schulreich et al. 2023](#)). It is commonly known as the Local Bubble, Local Cavity, or Local Chimney ([Welsh et al. 2004](#); [Puspitarini & Lallement 2012](#)). Since star formation tends to be concentrated, sequential supernovae are common ([Zucker et al. 2022](#); [Watkins et al. 2023](#); [Barnes et al. 2023](#); [Sandstrom et al. 2023](#)). Supernova explosions sweep up matter and magnetic field lines, leaving behind low-density superbubbles on the order of hundreds of parsecs in diameter ([Kim &](#)

[Ostriker 2015](#)). The swept-up matter is compressed into a shell surrounding the expanding superbubble, which is thought to trigger the formation of dense gas and stars ([Elmegreen 2011](#); [Dawson 2013](#); [Inutsuka et al. 2015](#)).

Thus, it is reasonable to expect that the formation of the Local Bubble dramatically influenced the magnetic field geometry in the nearby ISM. Some studies have aimed at modeling the geometry of the wall of cold neutral gas and dust surrounding the Local Bubble (e.g., [Alves et al. 2018](#); [Pelgrims et al. 2020](#)). Since the geometry of the magnetic field affects the measured dust polarization fraction, we search for an imprint of the Local Bubble geometry on the dust polarization fraction in this paper.

Additionally, one of the probes of the 3D spatial distribution of the neutral ISM is dust extinction toward stars. This is due to the scattering and absorption of starlight by dust. The extinction of a star's apparent magnitude is correlated with the dust column density along the line of sight from the observer to that star. The Gaia survey provided accurate distances to more than a billion stars within a few kiloparsecs from the Sun. Combining this distance information with the level of extinction towards each star has been transformative for the construction of 3D maps of the differential dust extinction ([Lallement et al. 2019](#); [Leike et al. 2020](#); [Vergely et al. 2022](#); [Edenhofer et al. 2023](#)). We use several 3D dust maps to quantify the complexity of the spatial distribution of the dust along the line of sight. We use that to explore the relationship between the 3D dust distribution and the measured dust polarization fraction.

In this work, we investigate the relationship between the 3D geometry of the nearby ISM and the dust polarization fraction. We start by introducing the data we use in Section 2. In Section 3, we search for an imprint of the Local Bubble geometry on the dust polarization fraction. In Section 4, we test how the dust polarization fraction is affected by the line-of-sight complexity of the dust. We discuss the implications of our results and conclude in Section 5.

## 2. DATA

### 2.1. *Planck* Data Products

We use the 80' R3.00 Planck data processed with the Generalized Needlet Internal Linear Combination (GNILC; [Remazeilles et al. 2011](#)) method at 353 GHz to remove the Cosmic Infrared Background (CIB) radiation from the Galactic dust emission ([Planck Collaboration et al. 2016a](#)). Following the fiducial offset corrections adopted by the Planck collaboration, we subtract  $452 \mu\text{K}_{\text{CMB}}$  from the GNILC total intensity map

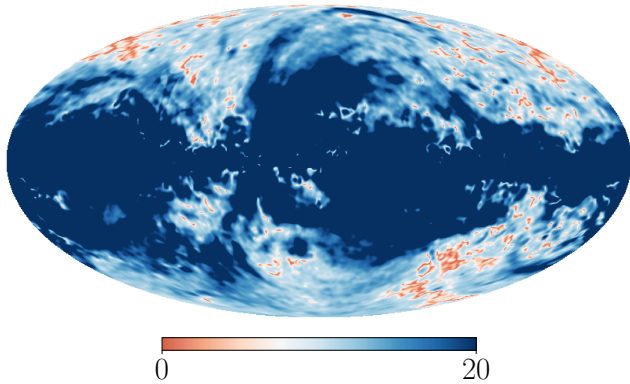


**Figure 1.** A map of the debiased signal-to-noise ratio of the Planck GNILC polarization fraction at  $80'$ . This is plotted with a diverging linear colorbar centered on 3, the cutoff we use as part of our sightline selections in Sections 3 and 4, with the allowed regions shown in blue.

to correct for the CIB monopole then add a Galactic offset correction of  $63 \mu\text{K}_{\text{CMB}}$  (Planck Collaboration et al. 2020a). Because the GNILC data are at  $\text{FWHM} = 80'$ , we downgrade the maps from their native HEALPix pixelization (Górski et al. 2005) at  $N_{\text{side}} = 2048$  to  $N_{\text{side}} = 64$ . We also use the R3.01 Planck data at 353 GHz, smoothed to  $80'$  as a cross-check (Planck Collaboration et al. 2020b). All of these maps use the COSMO polarization convention. We do not convert to the IAU polarization convention.

We use the modified asymptotic estimator of Plaszczynski et al. (2014) to debias the polarized intensity of the GNILC dust emission map and the associated uncertainty. We obtain a signal-to-noise ratio map of the dust polarization fraction,  $\text{SNR}_p$ , shown in Figure 1.

We estimate the total dust extinction over the full sky using Planck data products. Planck Collaboration et al. (2014) and Planck Collaboration et al. (2016a) fit a modified blackbody spectrum to the GNILC dust maps at different frequencies to estimate the dust temperature, spectral index, and optical depth over the sky. The dust optical depth is correlated with the reddening of quasars (Planck Collaboration et al. 2014). Using this observation, Planck Collaboration et al. (2016a) multiply the GNILC dust optical depth map by a factor of  $1.49 \times 10^{-4} \text{ mag}$  to construct a GNILC  $E(B - V)$  map. We query the publicly available `dustmaps` Python package (Green 2018) for the Planck Collaboration et al. (2016a) GNILC  $E(B - V)$  map. Assuming a standard extinction law, we multiply the GNILC  $E(B - V)$  map by 3.1 to obtain  $A_V^{\text{Planck}}$ .

## 2.2. 3D Dust Maps and Local Bubble Geometries

In Section 3, we use the 3D model of the Local Bubble surface geometry constructed by Pelgrims et al. (2020). To create this model, Pelgrims et al. (2020) extract distances to the first high dust density regions around the Sun from the 3D Cartesian map of dust differential extinction constructed by Lallement et al. (2019). They smooth the map of the distances to the Local Bubble surface by filtering out spherical harmonic modes above some threshold to remove small-scale fluctuations that might appear due to an inhomogeneous distribution of the dust density on the small scales. In this work, we use the map filtered to  $\ell_{\text{max}} = 10$ , which is the map used in their analysis. The Lallement et al. (2019) dust map is based on data from Gaia DR2 (Gaia Collaboration et al. 2018) and 2MASS (Skrutskie et al. 2006) and spans  $6 \times 6 \times 0.8 \text{ kpc}^3$  in the Heliocentric right-handed Galactic-XYZ coordinates. It has a voxel volume of  $125 \text{ pc}^3$  and a spatial resolution of 25 pc. Example slices of this map with the Pelgrims et al. (2020) model overplotted are shown in Figure 2.

We also use the 3D model of the Local Bubble surface constructed by O’Neill et al. (2024) for a brief investigation in Section 3. They use the 3D dust differential extinction provided by Edenhofer et al. (2023) to extract the distance to the Local Bubble in all directions as a region of higher dust density around the Sun.

In Section 4, we query the 12 posterior samples for the 3D dust maps provided by Edenhofer et al. (2023) via the publicly available `dustmaps` Python package (Green 2018) at their plane-of-sky native angular resolution of  $14'$ , which corresponds to a HEALPix pixelization scheme at  $N_{\text{side}} = 256$ . These 3D dust maps leverage distance and extinction estimates to stars from Zhang et al. (2023), which are derived from Gaia DR3 data (Gaia Collaboration et al. 2023). The distance resolution of these maps varies from 0.4 pc at 69 pc to 7 pc at 1.25 kpc. We query the map using uniform distance bins of 7 pc. The map is provided in unitless extinction values defined in Zhang et al. (2023). We multiply the map by a factor of 2.8 to convert it to Johnson’s  $V$ -band  $A'_V$  (Zhang et al. 2023). We then convert  $A'_V$  to volume density of hydrogen nuclei ( $n_{\text{H}}$ ) using the extinction curve from Fitzpatrick et al. (2019) to convert  $A_G = 0.796 A_V$  and the relationship  $A_G / N_{\text{H}} = 4 \times 10^{-22} \text{ cm}^2 \text{ mag}$  from Zucker et al. (2021) and Bialy et al. (2021). To match the resolution of the dust polarization fraction and smooth out small-scale fluctuations in the map, we smooth the HEALPix sphere at each distance bin to a  $\text{FWHM} = 80'$  then repixelate it to  $N_{\text{side}} = 64$ . Example slices of the raw map of the mean of the posterior samples are also

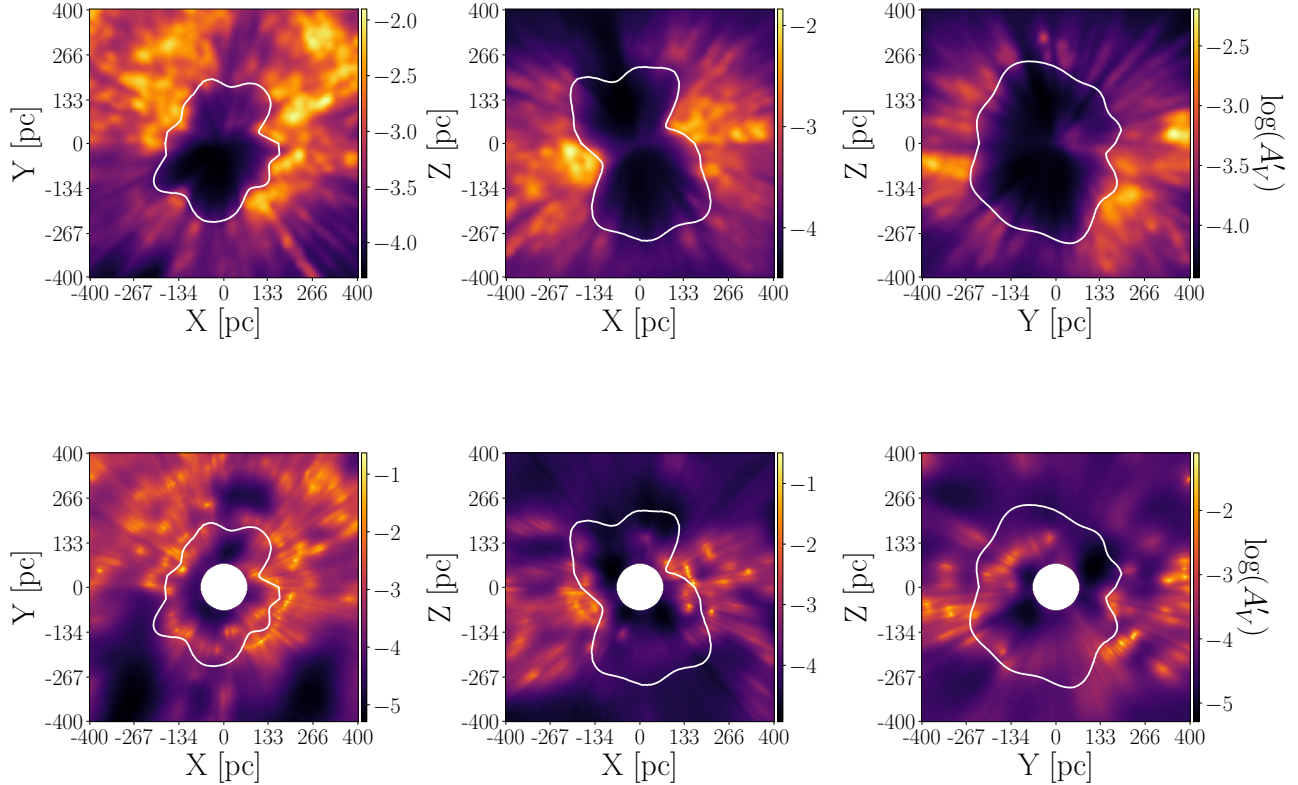


**Figure 2.** Slices through the XY (left), XZ (middle), and YZ (right) planes of the 3D reconstructed differential extinction maps of Lallement et al. (2019) (top) and Edenhofer et al. (2023) (bottom). The Sun is at the origin. The positive X axis points towards the Galactic center at  $l = 0^\circ$ , the positive Y axis points towards  $l = 90^\circ$  in the Galactic plane, and the positive Z axis points out of the plane in the direction of the Galactic North pole. The slices show the log of the differential extinction, which is in units of magnitudes per parsec. The subpanels only extend up to 400 pc in each direction for a direct comparison. The model for the Local Bubble surface geometry of Pelgrims et al. (2020) is overplotted in white in each subpanel. The white disk at the center of the bottom panel is due to missing data within 70 pc of the Sun in the Edenhofer et al. (2023) maps.

shown in Figure 2 with the Pelgrims et al. (2020) model overplotted for comparison.

In Section 4, we also make comparisons with the 3D dust maps provided by Leike et al. (2020). These maps leverage distance and extinction estimates from the StarHorse catalog (Anders et al. 2019), which combines data from Gaia DR2 (Gaia Collaboration et al. 2018), ALLWISE (Cutri et al. 2013), PANSTARRS (Flewelling et al. 2020), and 2MASS (Skrutskie et al. 2006). The Leike et al. (2020) maps span  $740 \times 740 \times 540 \text{ pc}^3$  in the Heliocentric Galactic-XYZ coordinates, respectively, with a voxel size of  $1 \text{ pc}^3$  and spatial resolution of 1 pc. We also query the 12 posterior samples of the Leike et al. (2020) maps via the `dustmaps` package. The Leike et al. (2020) maps are given in optical depth in the Gaia G band per 1 pc. We convert to  $n_H$  following Zucker et al. (2021) and Bialy et al. (2021).

### 2.3. Galactic Faraday Rotation Measure

We use the all-sky Galactic Faraday rotation measure (RM) map produced by Hutschenreuter et al. (2023)

for a brief investigation in Section 3. Using information field theory, a Bayesian inference framework for fields (Enßlin 2019), Hutschenreuter et al. (2023) disentangle the Galactic contribution to the RM from the compiled RM catalogs of polarized radio sources such as radio galaxies (Van Eck et al. 2023), supplemented by Galactic pulsar dispersion measures (Manchester et al. 2005), as well as data on Galactic bremsstrahlung emission (Planck Collaboration et al. 2016b) and the hydrogen  $\alpha$  spectral line (Finkbeiner 2003).

## 3. NO IMPRINT OF THE LOCAL BUBBLE ON THE DUST POLARIZATION FRACTION

### 3.1. Motivation

We begin the exploration of the effect of different geometrical factors on the dust polarization fraction by searching for an imprint of the geometry of the dust wall surrounding the Local Bubble on the Planck 353 GHz dust polarization fraction. In this subsection, we discuss the assumptions made in previous studies regarding the Local Bubble surface. These assumptions help us design

a test for studying this effect in the next subsection. A significant detection of an imprint of the Local Bubble geometry on the dust polarization fraction would validate these assumptions.

The first assumption is that the observed polarized dust emission is dominated by dust in the Local Bubble wall at the relevant angular scales and Galactic latitudes. This assumption, made in several analyses (e.g., [Alves et al. 2018](#); [Pelgrims et al. 2020](#); [O’Neill et al. 2023](#)), is supported by several studies using optical starlight polarization data ([Leroy 1999](#); [Andersson & Potter 2006](#); [Santos et al. 2011](#); [Frisch et al. 2015](#); [Medan & Andersson 2019](#); [Cotton et al. 2019](#); [Skalidis & Pelgrims 2019](#)). The alignment of neutral hydrogen structures at local velocities with starlight polarization toward stars at distances within a few hundred parsecs is consistent with a picture where most of these structures are positioned at comparable distances within the Local Bubble at high Galactic latitudes ( $|b| > 30^\circ$ ) ([Clark et al. 2014](#)). [Gontcharov & Mosenkov \(2019\)](#) observed that starlight polarization fraction plateaus after 150-250 pc across the sky. By comparing the 353 GHz polarized emission with the polarizing optical starlight, [Skalidis & Pelgrims \(2019\)](#) find that most of the 353 GHz polarized emission signal is captured within the first 250 pc at  $|b| > 60^\circ$ , suggesting the presence of a dust wall around that distance. They, however, find that this conclusion does not hold at  $30^\circ < |b| < 60^\circ$ .

The second assumption is that the magnetic field’s inclination is tangential to the surface of the Local Bubble, which stems from the model assumed for the formation of the Local Bubble. To fit a model of the Local Bubble magnetic field, [Alves et al. \(2018\)](#) and [Pelgrims et al. \(2020\)](#) assume that all the swept-up matter and field lines due to the supernova explosions that formed the Local Bubble are squeezed into a thin layer that follows its surface, leading the magnetic field lines to be tangent to the surface. [O’Neill et al. \(2023\)](#) also make this assumption to project the observed polarization angles of the dust emission onto the Bubble’s surface and build a 3D model of the Bubble wall magnetic field.

Other works have found magnetic field structure tangential to bubbles on supernova scales, observationally (e.g., [Kothes & Brown 2009](#); [West et al. 2016](#); [Tahani et al. 2022a,b](#)) and in simulations ([Kim & Ostriker 2015](#); [Maconi et al. 2023](#)). It has also been shown on the scales of HII regions, observationally ([Tahani et al. 2023](#)) and in simulations ([Krumholz et al. 2007](#)). On the scale of superbubbles, such as our Local Bubble, a comparison of the plane-of-the-sky and line-of-sight magnetic field strengths as well as measurements of the dust po-

larization fraction towards regions associated with the Orion-Eridanus superbubble suggest that the large-scale magnetic field in the region was primarily shaped by the expanding superbubble and is tangential to its surface ([Heiles 1997](#); [Soler et al. 2018](#)). However, there is no direct evidence that the nearby magnetic field is preferentially tangential to the Local Bubble surface.

The shape of the Local Bubble wall has been modeled differently in different works. Some studies fit a generalized parametric geometry, such as an ellipsoid ([Alves et al. 2018](#)), in an attempt to fit general properties of the Local Bubble magnetic field on large scales. Others model the detailed boundary of the Local Bubble using 3D maps of the dust extinction ([Pelgrims et al. 2020](#); [O’Neill et al. 2024](#)). These models therefore vary based on both the variations in the different 3D dust maps used as well as the methodology applied to these maps to define a Local Bubble surface. [Pelgrims et al. \(2020\)](#) model the radial distance of the Local Bubble wall from the Sun in each direction as the first distance where the second derivative with respect to the distance of the differential extinction constructed by [Lallement et al. \(2019\)](#) reaches zero, i.e., the first inflection point,  $d^2A'_V(r)/dr^2 = 0$ . [O’Neill et al. \(2023\)](#) and [Zucker et al. \(2022\)](#) use the geometry defined by [Pelgrims et al. \(2020\)](#) in their work. [O’Neill et al. \(2024\)](#) employ a similar methodology to [Pelgrims et al. \(2020\)](#), using the differential extinction maps constructed by [Edenhofer et al. \(2023\)](#) instead to construct their model. Other studies use different tracers to model the geometry of the Bubble. [Liu et al. \(2017\)](#) assumes that the measured X-ray intensity is proportional to the distance to the Bubble in the considered direction. Several other tracers such as NaI absorption measurements ([Sfeir et al. 1999](#); [Lallement et al. 2003](#)), stellar color excess measurements ([Lallement et al. 2014](#)), and diffuse interstellar bands ([Farhang et al. 2019](#)), have also been used for constructing models of the Bubble wall geometry. These geometries vary significantly from one to another. While some model the Local Bubble as a closed surface ([Pelgrims et al. 2020](#)), others describe the same structure as a Local Chimney, i.e., open in one or both directions away from the disk and funneling material into the Milky Way’s halo (e.g., [Heiles 1984](#); [Sfeir et al. 1999](#); [Lallement et al. 2003](#); [Marchal & Martin 2023](#); [O’Neill et al. 2024](#)). Also, the Local Bubble surface may have tunnels to surrounding cavities like the Gum Nebula and/or GSH238+00+09 rather than having a closed geometry (e.g., [Welsh 1991](#); [Lallement et al. 2003](#); [Marchal & Martin 2023](#); [O’Neill et al. 2024](#)).

We aim to test whether the degree-scale structure of the Local Bubble is measurably imprinted in the statis-

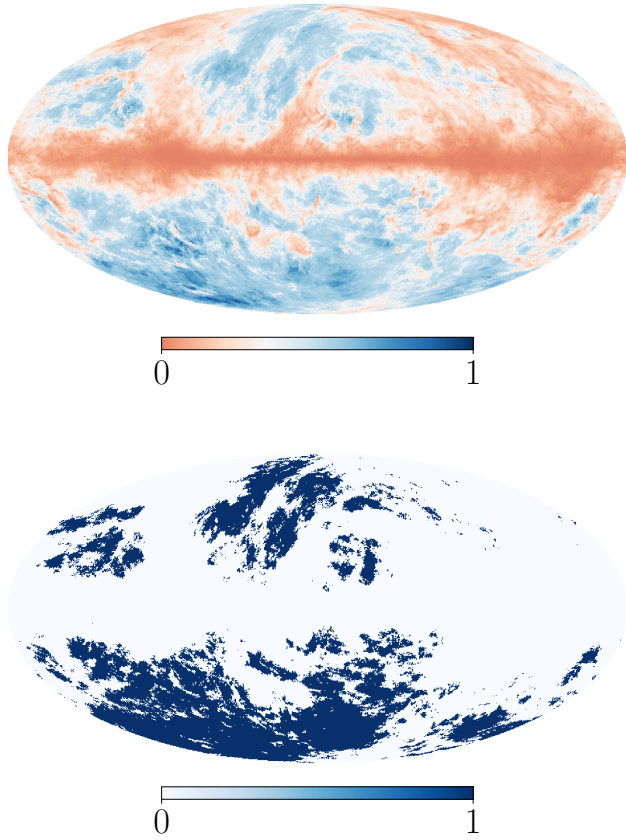


**Figure 3.** Maps used for selecting sightlines for the analysis described in Section 3. *Top panel:* A map of the ratio of the Lallement et al. (2019) 3D dust differential extinction map integrated within 50 pc of the Local Bubble surface defined by Pelgrims et al. (2020),  $A_V^{LB}$ , over the Planck dust extinction,  $A_V^{Planck}$ . This is plotted with a diverging colorbar centered on the 75th percentile (0.2), the cutoff we use in our sightline selection, with the allowed regions shown in blue. *Bottom panel:* A map of the mask of the selected region, combining  $A_V^{LB}/A_V^{Planck} > 0.2$  (top panel) with  $SNR_p > 3$  (Figure 1).

tics of polarized dust emission. We use the most recent models of the Local Bubble geometry constructed based on 3D dust mapping. For our main analysis, we use the Pelgrims et al. (2020) model, which has a closed geometry. However, we also perform a brief test using the O’Neill et al. (2024) model, whose geometry is not fully connected. In each case, we test whether a magnetic field that is tangential to the Local Bubble wall is a statistical driver of the observed variation in the dust polarization fraction.

### 3.2. Testing the Dependence of the Dust Polarization Fraction on the Magnetic Inclination Angle

Using 3D dust extinction maps and a model of the Local Bubble surface geometry, we can measure the angle between the line of sight and the local magnetic field orientation projected onto the Bubble’s surface in each direction. If the magnetic field lines were tangential to the Local Bubble surface as discussed in Section 3.1, the angle between the line of sight and the Bubble’s surface should on average be correlated with the measured dust polarization fraction along sightlines where the dust is concentrated in the Local Bubble wall. Therefore, by quantifying the correlation between this angle and the dust polarization fraction for different sightlines, we can test whether there is measurable evidence that the magnetic field traced by the dust polarization is preferentially tangential to the Local Bubble surface.

The magnetic inclination angle  $\gamma$ , i.e., the angle between the magnetic field orientation and the plane of the sky, affects the measured dust polarization fraction. The polarization fraction,  $p$ , is defined as

$$p = P/I = \sqrt{Q^2 + U^2}/I, \quad (1)$$

where  $P$  is the debiased polarized intensity as described in Section 2,  $Q$  and  $U$  are the Stokes parameters, and  $I$  is the total unpolarized intensity. Assuming uniform grain properties, the Stokes  $I$ ,  $Q$ , and  $U$  parameters of the dust emission can be written as (Fiege & Pudritz 2000; Padoan et al. 2001; Pelkonen et al. 2007)

$$I = \int \epsilon \rho ds - \frac{1}{2} \int \alpha \epsilon \rho \left( \cos^2 \gamma - \frac{2}{3} \right) ds, \quad (2)$$

$$Q = - \int \alpha \epsilon \rho \cos 2\psi \cos^2 \gamma ds, \quad (3)$$

$$U = - \int \alpha \epsilon \rho \sin 2\psi \cos^2 \gamma ds, \quad (4)$$

where  $\rho$  is the volume density,  $ds$  is a distance segment along the line of sight,  $\epsilon$  is the dust emissivity,  $\alpha$  is a coefficient defined in Equation 15 of Padoan et al. (2001) that is a product of polarization efficiency factors, such as the degree of dust alignment and the dust grain polarization cross-section, and  $\psi$  is the angle between the projection of the magnetic field on the plane of the sky and South, and the Stokes parameters are given in the COSMO polarization convention. These equations show the dependence of the dust polarization fraction on  $\gamma$ ,  $\psi$ ,  $\alpha$ ,  $\rho$ , and  $\epsilon$  and their variations along the line of sight. At large angular scales and away from the Galactic plane, the variation in the observed dust polarization fraction is dominated by  $\gamma$  and  $\psi$  (Hensley et al. 2019; Planck Collaboration et al. 2020a).

To maximize the chances of detecting this correlation, we limit our analysis to sightlines where the

dust in the Local Bubble wall contributes the most to the total extinction and where we have high signal-to-noise ratio measurements of the dust polarization fraction ( $\text{SNR}_p > 3$ ; Figure 1). We then select sightlines in the highest quartile of  $A_V^{\text{LB}} / A_V^{\text{Planck}}$ , i.e., sightlines where the extinction in the Local Bubble wall has the highest contribution to the total observed extinction (Section 2.1). For  $A_V^{\text{LB}}$ , we integrate the 3D dust differential extinction maps of Lallement et al. (2019) in the Local Bubble wall. We integrate over 50 pc in each direction, starting with the distance to the inner Local Bubble surface as defined by the 3D model of Pelgrims et al. (2020). Note that the threshold that corresponds to the highest quartile is  $A_V^{\text{LB}} / A_V^{\text{Planck}} \sim 0.2$ . This does not necessarily mean that  $\gtrsim 20\%$  of the total extinction is attributable to the Local Bubble wall, as the integration over 50 pc may not represent the true Bubble thickness for all sightlines, and  $A_V^{\text{Planck}}$  is estimated through a scale factor multiplied by the GNILC dust optical depth map (Section 2.1). Nevertheless, this represents a best estimate of the sky regions for which the Local Bubble wall accounts for the largest fraction of the total extinction. This map and the final mask are shown in Figure 3. While we define this mask to maximize the chance of detecting an imprint of the Local Bubble wall on the dust polarization, we also perform this analysis with different masks. If we redefine  $A_V^{\text{Planck}}$  using the integral from the Local Bubble surface to 100 pc, rather than 50 pc, 97% of the selected sightlines remain identical. The threshold that corresponds to the highest quartile increases to  $A_V^{\text{LB}} / A_V^{\text{Planck}} \sim 0.4$  in this case. We additionally perform this analysis with masks based on simple latitude cuts, including one focusing only on sightlines with  $|b| > 60^\circ$ . We find that the conclusions in Section 3.4 do not change for these different masks.

### 3.3. Magnetic Fields in the Local Bubble Wall

We perform the following steps to estimate the angle between the line of sight and the Local Bubble wall.

1. For the Local Bubble geometry, we use the 3D model developed by Pelgrims et al. (2020). Since this model is constructed based on the 3D dust map of Lallement et al. (2019), we use this dust map in this subsection. Example slices of the map with the model overlaid are shown at the top of Figure 2. The resolution of this dust map is 25 pc. We use a 3D Gaussian kernel with a standard deviation of 25 pc to smooth the data as done in Pelgrims et al. (2020). This smooths out spurious small-scale fluctuations in the data product that may affect the results.

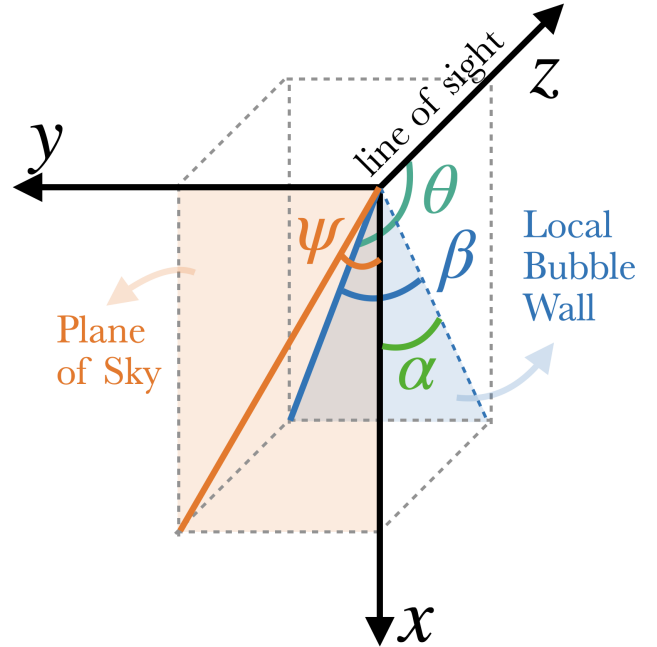


**Figure 4.** Diagram of the angles described and used in Section 3.3 for projecting the plane-of-sky magnetic field orientation (orange line) onto the Local Bubble wall (blue). The coordinates in this diagram follow the COSMO (HEALPix) convention, which is used in the Planck GNILC maps. These are not the Galactic coordinates used in Figure 2. For each position in the sky looking outwards, the local x-axis points South, the local y-axis points East, and the local z-axis points outwards.

2. We calculate the gradient of the differential extinction data cube,  $\nabla A'_{V,i}$  for each voxel  $i$ . This is a vector in the direction of the steepest change in the 3D volume at a given voxel. For the voxels at the surface of the Local Bubble wall,  $\nabla A'_{V,i}$  would therefore be orthogonal to that surface.
3. For each voxel  $i$ , we calculate the angle between the Local Bubble surface when projected onto the  $x - z$  plane and the plane of the sky as

$$\alpha_i = \arccos \left( \frac{\nabla A'_{V,i} \cdot \vec{r}_i}{|\nabla A'_{V,i}| |\vec{r}_i|} \right), \alpha_i \in [0, \pi/2], \quad (5)$$

where  $\vec{r}_i$  is the line of sight vector, using the Sun, which is at the center of the data cube, as the origin. This angle is shown in Figure 4 in green.

4. Pelgrims et al. (2020) models the distance to the Local Bubble surface for each direction on a HEALPix sphere. We sample our 3D Cartesian cube of  $\alpha_i$  at the radial distance defined by the Pelgrims et al. (2020) model for each line-of-sight direction with a HEALPix pixelization scheme.

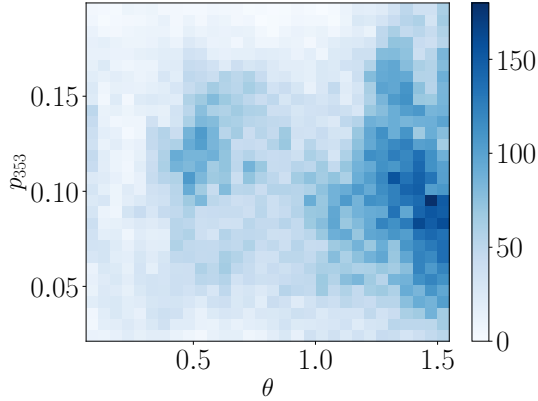


**Figure 5.** A 2D histogram showing the joint distribution of the dust polarization fraction and  $\theta$ , the angle between the line of sight and the plane tangent to the surface of the Local Bubble (Equation 8) for the sightlines within the mask in Figure 3. There is no significant correlation between these two quantities.

5. Using the Planck GNILC Stokes  $Q$  and  $U$  maps at 353 GHz, we calculate the plane-of-sky magnetic field orientation as

$$\psi = \frac{1}{2} \arctan \frac{-U}{-Q}. \quad (6)$$

This angle is shown in Figure 4 in orange.

6. We project the plane-of-sky magnetic field orientation onto the Local Bubble surface as

$$\beta = \arctan(\tan \psi \cos \alpha). \quad (7)$$

This angle is shown in Figure 4 in blue.

7. We calculate the angle between the line of sight and the magnetic field lines tangential to the surface of the Local Bubble as

$$\theta = \arccos(\cos \beta \sin \alpha). \quad (8)$$

This angle is shown in Figure 4 in teal.

### 3.4. No Detected Imprint of the Local Bubble Wall on the Dust Polarization Fraction

We do not find any correlation between  $p_{353}$  and  $\theta$  from Equation 8 over the mask defined in Figure 3. The joint distribution is shown as a 2D histogram in Figure 5. The Spearman rank coefficient, which is agnostic to the functional dependence between  $p_{353}$  and  $\theta$ , is  $3 \times 10^{-3}$ . This lack in correlation persists for each of the masks described in Section 3.2. This indicates that at least one of the assumptions described in Section 3.1 is not valid. In other words, either the magnetic field is not

generally tangent to the Local Bubble surface, the dust polarization is not dominated by the dust within 50 pc of the surface as defined by the Pelgrims et al. (2020), or a combination of these possibilities.

We also test whether we find an anti-correlation between  $\theta$  and the absolute value of the Faraday rotation measure (Section 2.3) but do not find any evidence for it. Therefore, we do not find an imprint of the detailed 3D geometry of the Local Bubble wall on the polarization statistics.

O’Neill et al. (2024) provide a map of the inclination angle between the Local Bubble wall as defined by their model and the plane of the sky. We also test for a correlation between this angle and the dust polarization fraction. We use a similar sightline selection criterion, replacing the Lallement et al. (2019) map with the Edenhofer et al. (2023) map and the Pelgrims et al. (2020) model with the O’Neill et al. (2024) model. We calculate a Spearman rank coefficient of 0.04, i.e., we do not find any correlation.

## 4. IMPRINT OF DUST COMPLEXITY ON DUST POLARIZATION FRACTION

We continue the investigation of how the 3D distribution of dust impacts the dust polarization fraction beyond the Local Bubble, taking into account the distribution of the dust in an extended volume around the Sun. We use the 3D dust maps constructed by Edenhofer et al. (2023) in this section. The benefits of these maps are that they have high resolution and extend radially up to 1.25 kpc away from the Sun.

If contributions to the polarized dust emission originate from regions along the line of sight with differently oriented magnetic fields, the integrated signal will be depolarized relative to emission from a region with uniform magnetic fields. We postulate that sightlines with multiple dust components that are separated in distance and contribute similarly to the total column density are more likely to have substantial dust emission originating from regions with differently oriented magnetic fields. We test the hypothesis that on average, for sightlines with the same column density, the ones for which the dust is distributed into multiple components at different distances with similar contributions to the total column density are associated with higher levels of depolarization than those for which the dust contribution to the total column density is concentrated. Another way to state our hypothesis is that given two sightlines at the same column density, the one with a more complex 3D dust distribution will have a lower dust polarization fraction on average.



#### 4.1. Sightline Selection

We select sightlines with high-fidelity dust polarization measurements ( $\text{SNR}_p > 3$ ), that pass through regions with trustworthy 3D dust reconstruction, and that have a dominant contribution from the dust extinction within the 3D dust maps  $A_V^{\text{Edenhofer}}$  to the total estimated extinction  $A_V^{\text{Planck}}$  (Section 2.1). The last constraint is to avoid sightlines at the lowest Galactic latitudes, where the dust extends in distance well beyond the regions where the dust is mapped in 3D out to 1.25 kpc. We mask sightlines where the ratio  $A_V^{\text{Edenhofer}}/A_V^{\text{Planck}} < 0.5$ .

Edenhofer et al. (2023) use estimates of stellar distances and extinctions from Zhang et al. (2023) to construct their 3D dust maps. However, Edenhofer et al. (2023) found that their estimated extinction disagrees with Zhang et al. (2023) where the radially integrated differential extinction is below 50 mmag or above 4 mag. We therefore use those thresholds to mask sightlines where the dust differential extinction is likely to be significantly over- or under-estimated. The distance to those thresholds for a given sightline varies slightly for the 12 different posterior samples, so we apply a slightly different mask to each posterior sample. We only consider sightlines where the differential extinction integrated radially outwards reaches 50 mmag within 200 pc of the Sun. A threshold higher than 200 pc would include more sightlines in the selection, but it would shorten the minimum path length considered. Because in Section 4.5, we compare our results with the Leike et al. (2020) maps, which only extend out to 270 pc, we find 200 pc to be a good balance between having a large enough sample size and minimum path length. The minimum path length considered through the Edenhofer et al. (2023) maps for estimating the dust complexity is therefore 1.05 kpc.

A map of the distance at which the extinction reaches 50 mmag for different sightlines is shown at the top of Figure 6. This is for the first posterior sample, but the equivalent maps for the remaining 11 posterior samples look visually indistinguishable. We center the diverging colorbar in this subplot to 200 pc to show which sightlines pass the threshold.

After masking sightlines with  $\text{SNR}_p < 3$  or with  $A_V^{\text{Edenhofer}}/A_V^{\text{Planck}} < 0.5$  for the 12 posterior samples, the integrated differential extinction within 1.25 kpc is higher than 4 mag for only about 10 sightlines per posterior sample. We exclude these sightlines from our analysis.

After performing all the cuts, we are left with about 19,100 sightlines per posterior sample ( $\sim 40\%$  of the sky) for this analysis. Those sightlines are shown at

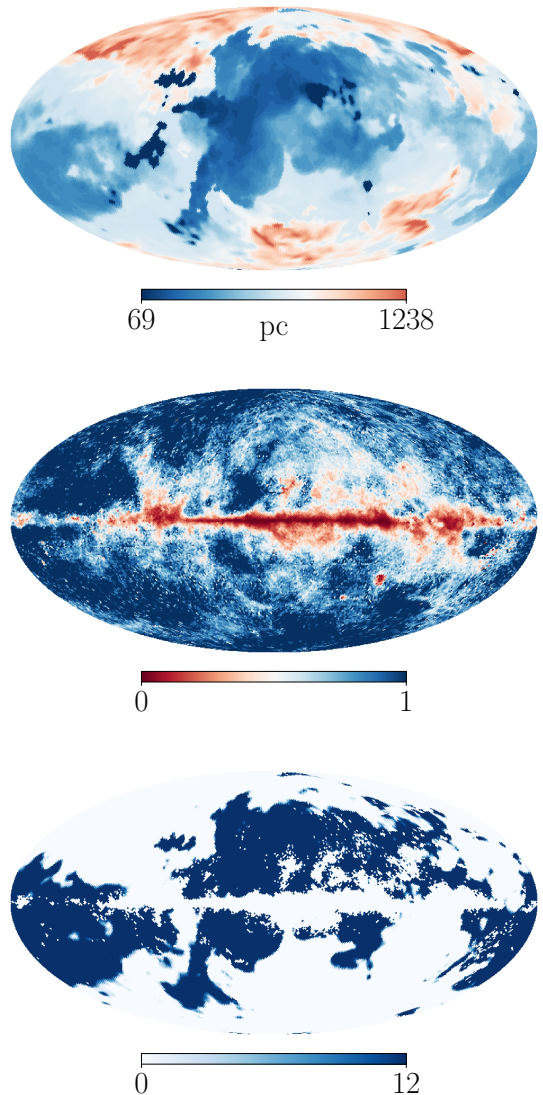


**Figure 6.** Maps used for selecting sightlines for the analysis described in Section 4. *Top panel:* A map of the distance at which the extinction in the first posterior sample of the Edenhofer et al. (2023) 3D dust maps reaches 50 mmag. This is plotted with a diverging colorbar centered on 200 pc, the cutoff we use in our sightline selection, with the allowed regions shown in blue. *Middle panel:* A map of the ratio of the Edenhofer et al. (2023) 3D dust differential extinction map integrated out to 1.25 kpc over the Planck dust extinction. This is plotted with a diverging colorbar centered on 0.5, the cutoff we use in our sightline selection, with the allowed regions shown in blue. *Bottom panel:* A sum of the masks of the selected regions over each of the 12 posterior samples, combining the selected regions from the quantities in the top panel, middle panel, and Figure 1.

the bottom of Figure 6. The map shown is the sum of the binary masks over the 12 posterior samples. Note that

the only discrepancies between the 12 posterior samples are at the edges of the selected regions. The rest of the map is either 12 or 0.

#### 4.2. Dust Complexity

We aim to quantify the complexity of the 3D dust distribution along each line of sight. For this, we take inspiration from [Panopoulou & Lenz \(2020\)](#), who perform a Gaussian decomposition of the neutral hydrogen (H I) emission spectra of each sightline to quantify its complexity. They use these components  $i$ , weighted by their column density  $N_{\text{HI}}^i$ , to define a metric

$$\mathcal{N}_c^{\text{HI}} = \sum_{i=1}^{n_{\text{clouds}}} \frac{N_{\text{HI}}^i}{N_{\text{HI}}^{\text{max}}}, \quad (9)$$

where  $N_{\text{HI}}^{\text{max}}$  is the column density of the component with highest  $N_{\text{HI}}$ . This is a more relevant measurement of complexity than simply counting the number of components because it takes into account the relative contribution of each detected component, and the dust polarization signal arises from a density-weighted integral along the line of sight. If there are two components along the line of sight and they have equal column densities, then  $\mathcal{N}_c^{\text{HI}} = 2$ , whereas if one has half the column density of the other, then  $\mathcal{N}_c^{\text{HI}} = 1.5$ , and so forth. Therefore,  $\mathcal{N}_c^{\text{HI}}$  could be, for instance, 2 for any number of components larger than 1. This metric was used to detect an imprint of line-of-sight magnetic field tangling in dust polarization in [Pelgrims et al. \(2021\)](#).

We use a metric inspired by Equation 9 to quantify the complexity of the 3D dust distribution, i.e., we decompose the 3D dust sightlines into “clouds,” or components along the line of sight, and then use a version of Equation 9, replacing  $N_{\text{HI}}$  with  $N_{\text{H}}$  inferred from the dust extinction (Section 2), i.e.,

$$\mathcal{N}_c = \sum_{i=1}^{n_{\text{clouds}}} \frac{N_{\text{H}}^i}{N_{\text{H}}^{\text{max}}}. \quad (10)$$

To decompose each of the 19,100 sightlines into different components, we use the dendrogram technique ([Rosolowsky et al. 2008](#)). We use the Python package `astrodendro`<sup>1</sup>. [Cahlon et al. \(2023\)](#) applied the 3D version of this technique on the [Leike et al. \(2020\)](#) 3D dust maps to produce a uniform catalog of molecular clouds in the Solar neighborhood. In this analysis, we apply the 1D version on individual sightlines.

Dendrogramming identifies density peaks in the data and connects them along hierarchical isosurfaces of constant  $n_{\text{H}}$ , forming a tree-like structure. We refer the

reader to [Rosolowsky et al. \(2008\)](#) for a description of the core algorithm. We focus the explanation here on the algorithm’s three parameters. The first parameter defines the minimum absolute Hydrogen number density  $n_{\text{H}}$  threshold for a structure to be included as part of the tree. We set this parameter to 0. This is because the tree-like structure constructed by this algorithm is not useful for our purposes. We only consider the density peaks identified.

The remaining two parameters,  $\Delta_n$  and  $\#_{\text{voxels}}$ , define the minimum prominence for a peak to be considered an independent component. Its largest  $n_{\text{H}}$  has to be  $\Delta_n$  above the  $n_{\text{H}}$  of the adjacent isosurface for it to be considered an independent component from that isosurface. Similarly,  $\#_{\text{voxels}}$  defines the threshold number of voxels it has to span along a sightline to be considered an independent component, where each voxel spans 7 pc of the sightline. If a peak passes both of those thresholds, it is identified as a component by the algorithm.

For this analysis, we experiment with various values for  $\Delta_n$  and  $\#_{\text{voxels}}$  and plot the resulting peaks identified for each variation. We find a range between  $\Delta_n = 1.94 \times 10^{-3} \text{ cm}^{-3}$  ( $A'_V = 3 \times 10^{-6} \text{ mag/pc}$ ) and  $\Delta_n = 3.87 \times 10^{-3} \text{ cm}^{-3}$  ( $A'_V = 9 \times 10^{-6} \text{ mag/pc}$ ) and between  $\#_{\text{voxels}} = 3$  (21 pc) and  $\#_{\text{voxels}} = 5$  (35 pc) recovers the visually identified peaks. We report our results for the fiducial values of  $\Delta_n = 4.52 \times 10^{-3} \text{ cm}^{-3}$  ( $A'_V = 7 \times 10^{-6}$ ), and  $\#_{\text{voxels}} = 3$  (21 pc). However, we find our results to be robust to all the variations we test for within the ranges mentioned.

We run the dendrogram algorithm on each sightline separately, considering the entire sightline from 69 pc to 1.25 kpc. However, we only keep identified components with peaks that are radially farther than the distance at which the extinction in that sightline reaches 50 mmag (Section 4.1). If the distance of the peak of a component is farther than this threshold but part of the component is below that threshold (Figure 7), we still consider the part of the component that is below that threshold when integrating over the  $n_{\text{H}}$  of that component. We find that the peak with the highest dust column density lies within 270 pc from the Sun for most sightlines within our mask.

We calculate Equation 10 for each sightline to quantify its dust complexity. For the sightline in Figure 7, for example,  $\mathcal{N}_c=2.16$ . We show a map of  $\mathcal{N}_c$  for the sightlines we select in Section 4.1 for one of the 12 pos-

<sup>1</sup> <http://www.dendrograms.org/>

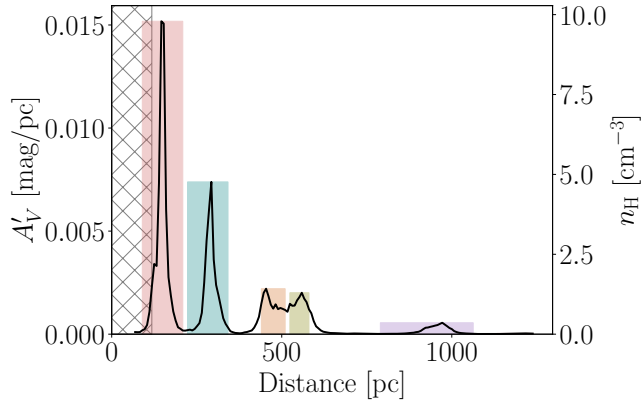


**Figure 7.** The dust distribution in units of differential extinction (mag/pc, left y-axis) and equivalent Hydrogen number density ( $\text{cm}^{-3}$ , right y-axis) along a representative sightline through the Edenhofer et al. (2023) maps. The Galactic coordinates of this sightline are  $l = 163.12^\circ$  and  $b = -11.42^\circ$ . The region before the extinction reaches 50 mmag (hatched) is discarded from our analysis. The components identified by the dendrogram algorithm with  $\Delta_n = 4.52 \times 10^{-3} \text{ cm}^{-3}$  ( $A'_V = 7 \times 10^{-6}$ ), and  $\#_{\text{voxels}} = 3$  (21 pc) are shaded in different colors.

terior samples of the Edenhofer et al. (2023) maps at the top of Figure 8.<sup>2</sup>

#### 4.3. Nearest-Neighbor Matching

To examine the effect of line-of-sight dust complexity on the dust polarization fraction, we compare sightlines that have the same total column densities but very different 3D dust distributions. We define low- and high-dust complexity sightlines as sightlines with  $\mathcal{N}_c \leq 1.1$  and  $\mathcal{N}_c \geq 1.5$ , respectively. The goal is to compare sightlines with different dust distributions, so the particular  $\mathcal{N}_c$  threshold values are less important. We start with these values for our fiducial analysis because they are similar to the thresholds used in Pelgrims et al. (2021). The Pelgrims et al. (2021) analysis used a Gaussian decomposition of 3D maps of the neutral hydrogen emission line, where the third dimension is radial velocity. They used  $\mathcal{N}_c=1$  and  $\mathcal{N}_c \geq 1.5$  in their analysis. However, for the data and mask we use in our analysis, we find that across the 12 posterior sample maps from Edenhofer et al. (2023), only 8-31 sightlines have  $\mathcal{N}_c=1$ , i.e., a single dust component. Since this does not represent a large enough sample size, we define the low-complexity bin as sightlines with  $\mathcal{N}_c \leq 1.1$ . This increases the number of sightlines in that bin to

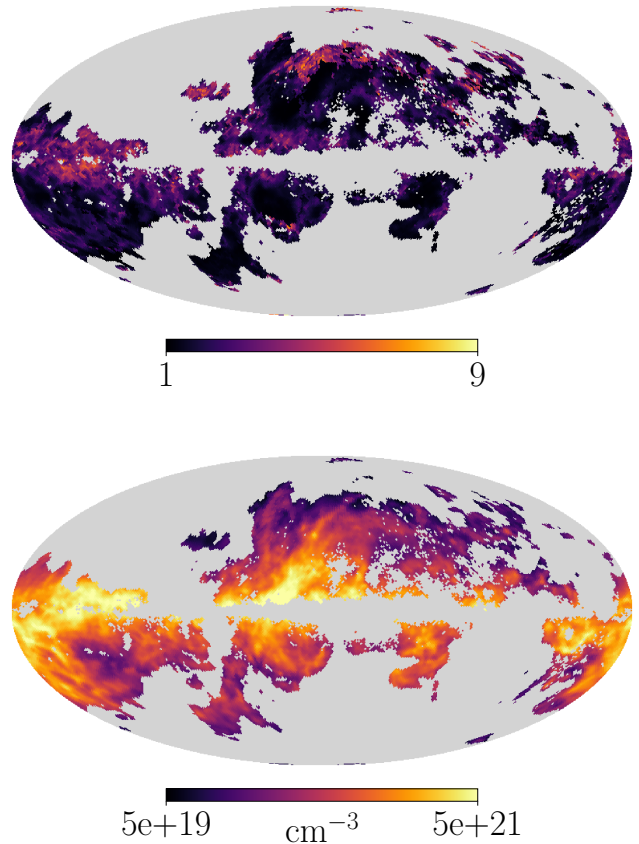


**Figure 8.** *Top panel:* A map of  $\mathcal{N}_c$  calculated using the dendrogram algorithm with  $\Delta_n = 4.52 \times 10^{-3} \text{ cm}^{-3}$  ( $A'_V = 7 \times 10^{-6}$ ), and  $\#_{\text{voxels}} = 3$  (21 pc). *Bottom panel:* A log-scale map of  $N_{\text{H}}^{\text{Edenhofer}}$  formed by integrating over the entire dataset (up to 1.25 kpc) with units of  $\text{cm}^{-2}$ . These maps are shown only for the sightlines selected in Section 4.1 and for one of the posterior samples of Edenhofer et al. (2023).

around 1,000 per posterior sample. The number of sightlines in the  $\mathcal{N}_c \geq 1.5$  bin is around 13,000. However, we also confirm that our results are robust to variations in these thresholds (Section 4.6).

Because the  $\mathcal{N}_c$  bins are widely separated, small fluctuations in  $\mathcal{N}_c$  due to the choices of  $\Delta_n$  and  $\#_{\text{voxels}}$  do not cause sightlines from one bin to shift to the other bin. However, we also verify that our results are robust to different choices of  $\Delta_n$  and  $\#_{\text{voxels}}$ .

We treat the column density as a confounding variable when comparing the distribution of  $p_{353}$  for the low- and high-complexity bins. Any difference in the  $p_{353}$  distributions for the low- and high-complexity bins could potentially be explained by a difference in the column density integrated over the distance used to calculate  $\mathcal{N}_c$

<sup>2</sup> We make the  $\mathcal{N}_c$  maps for the 12 posterior samples of Edenhofer et al. (2023) publicly available at <https://doi.org/10.7910/DVN/IW09AE> (Halal et al. 2024)

or a difference in the total column density over a sightline. Therefore, both need to be taken into account for a fair comparison of  $p_{353}$  between the two complexity bins.

We integrate  $n_{\text{H}}$  for each sightline up to 1.25 kpc, starting from either the distance at which the extinction reaches 50 mmag or the minimum distance of the first detected component whose peak lies farther than that distance as explained in Section 4.2, whichever is closer. We call this  $N_{\text{H}}^{\text{Edenhofer}}$  and show a map of it for the sightlines considered in our analysis in the bottom panel of Figure 8.

Since  $N_{\text{H}}^{\text{Edenhofer}}$  only takes into account dust up to 1.25 kpc, we also consider the total column density over a sightline. We convert  $A_V^{\text{Planck}}$  (Section 2.1) to  $N_{\text{H}}^{\text{Planck}}$  following the formalism in Section 2.2. In Section 4.6, we also experiment with adding the absolute value of the Galactic latitude as an additional confounding variable.

We perform nearest-neighbor matching with no replacement between the sightlines in the low- and high-complexity bins. We pair up each low-complexity sightline to the high-complexity sightline with the closest  $N_{\text{H}}^{\text{Edenhofer}}$  and  $N_{\text{H}}^{\text{Planck}}$  values based on the Manhattan distance using the ball-tree algorithm. The number of pairs is, therefore, equal to the number of sightlines in the low-complexity group, which is the smaller group. For each matched pair, we subtract the  $p_{353}$  of the sightline with the lower complexity from the  $p_{353}$  of the sightline with the higher complexity. We take the average of the differences over the matched pairs,  $\Delta p_{353}$ , to test whether sightlines with higher dust complexity have higher depolarization levels on average than sightlines with lower dust complexity, i.e.,  $\Delta p_{353} < 0$ .

#### 4.4. Statistical Tests

We determine the statistical significance of our results through permutation tests. We perform the analysis described in Section 4.3 and obtain  $\Delta p_{353}^s$  as the mean over the pairs for each of the 12 posterior samples  $s$ . We perform a permutation-based null test in which we randomly choose one sightline to subtract from the other in each pair, rather than always subtracting  $p_{353}$  of the low-complexity sightline. We repeat this 10,000 times and obtain a distribution of  $\Delta p_{353}^{s, \text{null}}$  for each posterior sample  $s$ . We calculate a p-value as the proportion of  $\Delta p_{353}^{s, \text{null}}$  that are equal to or more extreme than  $\Delta p_{353}^s$ .

We additionally use an alternative null test. Instead of separating sightlines into high- and low-complexity groups, we randomly select 25% of sightlines (5,050 sightlines) to be in one group and 25% to be in the other

group. We then run the same analysis on those 2 groups, pairing them up based on  $N_{\text{H}}^{\text{Edenhofer}}$  and  $N_{\text{H}}^{\text{Planck}}$  and subtracting  $p_{353}$  of one group from that of the other for each pair. To ensure we are not biasing the null test by matching neighboring sightlines which may have similar  $p_{353}$ , for each run, we randomly alternate between selecting the sightlines in one group to be in the Northern Galactic hemisphere and the sightlines in the other group to be in the Southern Galactic hemisphere and the other way around. We find that sightlines in the Northern Galactic hemisphere tend to have higher  $p_{353}$  on average than sightlines in the Southern Galactic hemisphere, so  $\Delta p_{353}^{s, \text{null}}$  will be biased towards positive or negative values based on which of the two groups is selected from which hemisphere. Using this version of the null test, therefore, takes this bias into account and yields a more conservative estimate of the significance of our hypothesis test. The permutation-based null test, however, guarantees the same number of pairs as the hypothesis test, so we use that version as the main null test when reporting the results. We find that our results are consistent regardless of which null test we use.

We consider results with a two-tailed p-value  $< 0.001$  to be statistically significant. We repeat this analysis for several reasonable values for  $\Delta_n$  and  $\#\text{voxels}$  and for different thresholds of the  $\mathcal{N}_c$  bins to ensure that our results are independent of those choices.

In addition to checking the statistical significance of  $\Delta p_{353}^s$  for each of the 12 posterior samples, we also report the mean and standard deviation of  $\Delta p_{353}^s$  across the posterior samples. The error propagated due to the uncertainty on  $p_{353}$  is 2 orders of magnitude less than the result. The uncertainty is dominated by the scatter from the 12 posterior samples of the 3D dust map.

#### 4.5. Results

We perform the analysis described in the previous subsections on the [Edenhofer et al. \(2023\)](#) maps which extend radially to 1.25 kpc and compare the dust polarization fractions of sightlines with  $\mathcal{N}_c \leq 1.1$  and those with  $\mathcal{N}_c \geq 1.5$ . An example of a pair of matched sightlines with the same  $N_{\text{H}}^{\text{Edenhofer}}$  and  $N_{\text{H}}^{\text{Planck}}$  is shown in Figure 9. Even though the dust polarization fraction of the higher-complexity sightline is lower than that of the lower-complexity sightline in this example, not all sightlines follow this trend. We are only looking for a statistically significant average effect. An example of the distribution of the differences in  $p_{353}$  over all pairs in one of the map posterior samples is shown in Figure 10 along with the same distribution for the permutation-based null test.

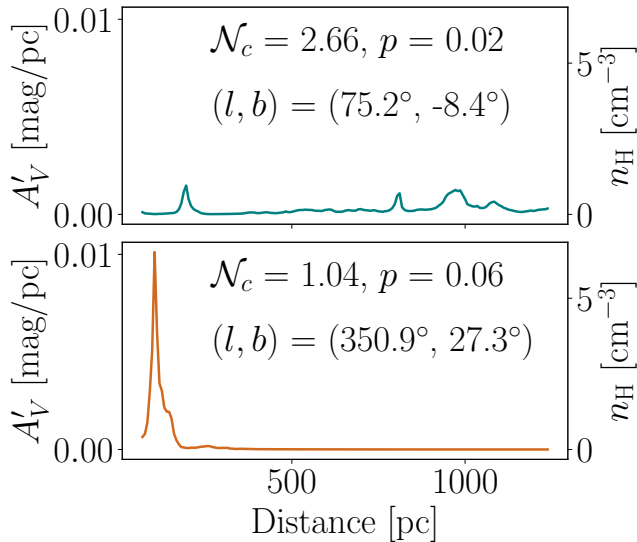


**Figure 9.** The dust distribution in units of differential extinction (mag/pc, left y-axis) and equivalent Hydrogen number density ( $\text{cm}^{-3}$ , right y-axis) along a pair of matched sightlines through the first posterior sample of the [Edenhofer et al. \(2023\)](#) map. These sightlines have the same  $N_{\text{H}}^{\text{Edenhofer}}$ , but the top one has a higher complexity than the bottom one. The Galactic coordinates, dust complexity, and dust polarization fraction of each of the sightlines are denoted on their subpanels.

For this test,  $\Delta p_{353}^s$ , the mean over the paired sightlines for each posterior sample  $s$ , is plotted in orange at the top of Figure 11. The mean and standard deviation of  $\Delta p_{353}^s$  over the 12 samples are  $-1.47 \times 10^{-2}$  and  $0.22 \times 10^{-2}$ , respectively. All 12 posterior samples pass both null tests described in Section 4.4 with a p-value  $< 0.001$ . A random  $\Delta p_{353}^{s, \text{null}}$  for each posterior sample is shown in blue at the top of Figure 11 as well. Therefore, we find that higher dust complexity at equivalent column densities is associated with depolarization at the 1.5% level. This is at the level of 6.8% of the maximum dust polarization fraction measured by [Planck Collaboration et al. \(2020a\)](#) at 353 GHz and  $80'$ .

To determine whether this result is uniquely enabled by the [Edenhofer et al. \(2023\)](#) dust maps since they extend radially to 1.25 kpc, we repeat the analysis using the 3D [Leike et al. \(2020\)](#) dust maps, which extend to 370 pc in the positive and negative Galactic-X and Y coordinates and 270 pc in the positive and negative Galactic-Z coordinate. For consistency between different sightlines in those maps, we truncate all sightlines at 270 pc. Also, we start each sightline at 70 pc since [Leike et al. \(2020\)](#) find that the reconstructed dust density closer than 70 pc resembles a smeared-out version of the farther dust, an artifact related to systematic data biases. [Leike et al. \(2020\)](#) also provide 12 posterior sam-

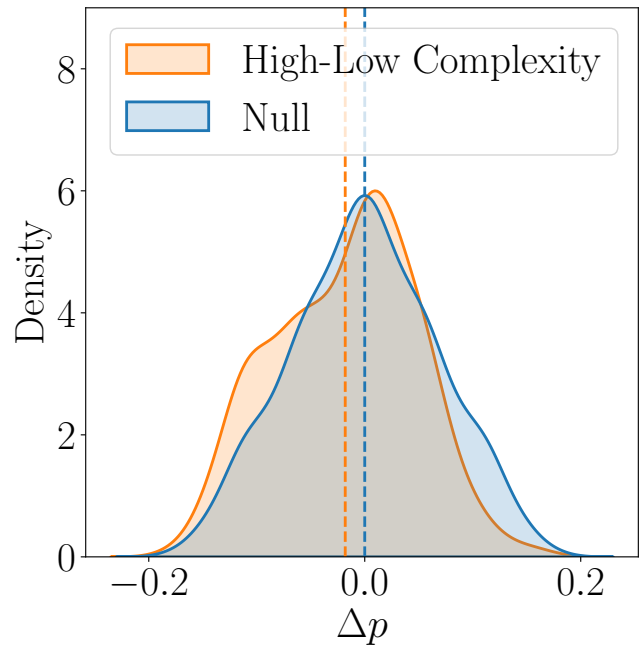


**Figure 10.** Kernel density estimate plots of the  $\Delta p_{353}$  distributions over all matched pairs of sightlines of one posterior sample of the [Edenhofer et al. \(2023\)](#) maps. The  $p_{353}$  of the lower complexity sightline is always subtracted from that of the higher complexity one in the orange distribution. This has a mean of  $\Delta p_{353} = -1.81 \times 10^{-2}$ , which is plotted as an orange dot in Figure 11. The blue distribution contains the same pairs as the orange one with the sign randomly flipped for each pair, i.e., the distribution of the permutation-based null test described in Section 4.4.

ples for their maps which we use for this analysis. Because we sample these data in increments of 2 pc as opposed to 7 pc as in the case of the [Edenhofer et al. \(2023\)](#) data, we set the dendrogram parameter  $\#_{\text{voxels}} = 10$ , which corresponds to 20 pc, compared to  $\#_{\text{voxels}} = 3$ , which corresponds to 21 pc in the case of the [Edenhofer et al. \(2023\)](#) data. We keep the dendrogram parameter  $\Delta_n$  the same for both maps. This results in about 3,500 sightlines with  $\mathcal{N}_c \leq 1.1$  and about 8,500 with  $\mathcal{N}_c \geq 1.5$ .

The results for repeating the analysis using the [Leike et al. \(2020\)](#) maps instead are shown at the bottom of Figure 11. The mean and standard deviation of  $\Delta p_{353}^s$  over the 12 posterior samples are  $2.75 \times 10^{-3}$  and  $3.06 \times 10^{-3}$ , respectively. None of the 12 samples pass either of the null tests described in Section 4.4, i.e., they are indistinguishable from the distributions of  $\Delta p_{353}^{s, \text{null}}$ . We also show a random  $\Delta p_{353}^{s, \text{null}}$  for each posterior sample in blue in the same subplot of Figure 11.

To determine whether the null result is attributed to using a different dataset or to the lower extent in radial

distance, we run the analysis on the [Edenhofer et al. \(2023\)](#) maps up to 270 pc, the same distance used for the [Leike et al. \(2020\)](#) maps. The number of sightlines with  $\mathcal{N}_c \leq 1.1$  and  $\mathcal{N}_c \geq 1.5$  after this distance cut are about 10,000 and 3,500, respectively. The difference in the  $\mathcal{N}_c$  distributions between this data and the [Leike et al. \(2020\)](#) maps is due to several differences in the maps and the post-processing we perform on them, including having to use slightly different dendrogram parameters and not counting components whose peak is closer than the distance where the differential extinction integrated radially outwards reaches 50 mmag in the [Edenhofer et al. \(2023\)](#) maps among other differences. We plot the results in the middle of Figure 11. The mean and standard deviation of  $\Delta p_{353}^s$  over the 12 posterior samples are  $1.05 \times 10^{-3}$  and  $1.36 \times 10^{-3}$ , respectively. Again, none of the 12 samples pass either of the null tests described in Section 4.4, i.e., they are indistinguishable from the distributions of  $\Delta p_{353}^{s, \text{null}}$ . The consistency of this result with null as well indicates that the null result we found using the [Leike et al. \(2020\)](#) maps is due to only considering distances up to 270 pc, not the choice of 3D dust dataset. This illustrates the role that dust components farther than 270 pc play in affecting polarization measurements.

#### 4.6. Validation

In this subsection, we summarize some of the tests we performed to verify our results. As described in Section 4.2, we find that our results are robust to reasonable variations in  $\Delta_n$  and  $\#\text{voxels}$ . These are summarized in Table 1 in Appendix A. The results are also consistent when using the Planck R3.01 353 GHz maps instead of the GNILC maps.

To ensure that the pairs were matched correctly, we examine the distributions of the differences in  $N_H^{\text{Edenhofer}}$  and  $N_H^{\text{Planck}}$  between the matched pairs. We verify that those differences peak near zero and are not skewed toward the positive or negative values. We find that to be the case for both variables and over all 12 posterior samples of [Edenhofer et al. \(2023\)](#). We also find our results to be robust when including  $|b|$  as an additional confounding variable to  $N_H^{\text{Edenhofer}}$  and  $N_H^{\text{Planck}}$  in the pair matching – in other words, the result is not attributable to a dependence of the dust polarization fraction on Galactic latitude. We show these results in Table 2 in Appendix A.

We also examine the angular separations between the sightline pairs and the discrepancies in their overall path lengths. The distributions of angular distances are consistent with a random distribution of angular distances for all 12 posterior samples of [Edenhofer et al. \(2023\)](#).

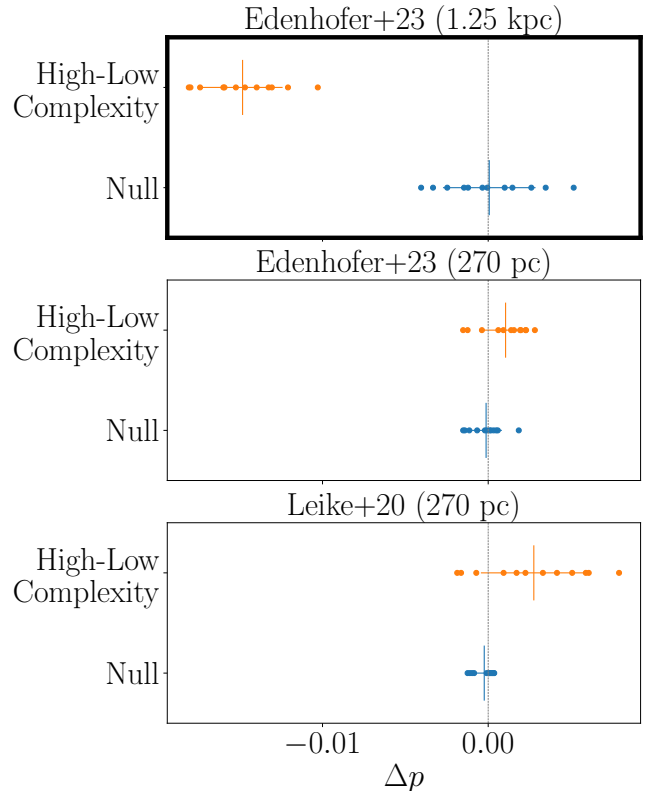


**Figure 11.** The mean difference in  $p_{353}$  over the paired sightlines for each of the 12 posterior samples, where for each pair,  $p_{353}$  for the lower-complexity sightline is subtracted from  $p_{353}$  for the higher-complexity sightline.  $\mathcal{N}_c$  is calculated on the [Edenhofer et al. \(2023\)](#) maps up to 1.25 kpc (top), the [Edenhofer et al. \(2023\)](#) maps up to 270 pc (middle), and the [Leike et al. \(2020\)](#) maps up to 270 pc (bottom). For each panel, the mean differences for the actual test are plotted in orange, and samples from the permutation-based null tests are plotted in blue. The mean and standard deviation of the 12 means for each test are also plotted. The top panel agrees with our hypothesis: that sightlines with similar column densities will, on average, exhibit lower dust polarization fractions when their 3D dust distribution is more complex.

We also find no significant differences in the total path lengths between the paired sightlines across all 12 samples.

We experiment with varying the  $\mathcal{N}_c$  thresholds that define the bin edges of the low- and high-complexity sightlines. The 25th and 75th percentiles of the  $\mathcal{N}_c$  distribution over our mask vary slightly over the 12 posterior samples of [Edenhofer et al. \(2023\)](#) and over variations in  $\Delta_n$  and  $\#\text{voxels}$ . However, they are roughly 1.4 and 2.3, respectively. Therefore, we split our sightlines based on these values into low- ( $\mathcal{N}_c \leq 1.4$ ) and high-complexity ( $\mathcal{N}_c \geq 2.3$ ) bins to achieve a roughly equal number of sightlines in each group. This should improve

the pair-matching outcomes since there are more sightlines to match from in the smaller group. We find that our results are robust to this change as shown in Table 1 in Appendix A.

Since neighboring sightlines are likely to have similar  $\mathcal{N}_c$  and similar  $p_{353}$  values, we test whether large regions of neighboring sightlines belonging to either the low- or high-complexity groups bias our results. We randomly sample 1,000 sightlines out of about 5,000 sightlines from each of the low- and high-complexity groups before pair matching, where we use  $\mathcal{N}_c \leq 1.4$  and  $\mathcal{N}_c \geq 2.3$  for these groups, respectively, in this case. We find that our results are robust to this test as shown in Table 3 in Appendix A.

Finally, we modify the definition of  $\mathcal{N}_c$  from Equation 10 to

$$\mathcal{N}_c = \frac{N_{\text{H}}^{\text{Edenhofer}}}{N_{\text{H}}^{\text{max}}}, \quad (11)$$

i.e., we use the total column density out to 1.25 kpc rather than a sum over the dust components in the numerator. With the new definition,  $\mathcal{N}_c$  is only sensitive to the dendrogram-identified component with the highest column density  $N_{\text{H}}^{\text{max}}$  rather than also being sensitive to the other dendrogram-identified components. Since the dendrogram parameters define the minimum prominence for a peak to be considered an independent component, we expect  $N_{\text{H}}^{\text{max}}$  to be the least sensitive component to those parameters. Therefore, the new definition is much less sensitive to the dendrogram parameters. The 25th and 75th percentiles of this modified version of  $\mathcal{N}_c$  are about 0.05 and 0.09 for the 12 posterior samples, and we use these as the upper and lower thresholds for the low- and high-complexity bins, respectively. Over the 12 posterior samples, we find a mean and standard deviation of  $\Delta p_{353} = 0.96 \times 10^{-2} \pm 0.34 \times 10^{-2}$ . This passes the null test with a p-value  $< 0.001$ .

## 5. DISCUSSION AND CONCLUSIONS

In this paper, we explore how different geometrical factors affect the fractional polarization of the dust emission. In Section 3, we test whether we detect an imprint of the Local Bubble geometry on the dust polarization fraction. Following the well-motivated assumptions that the magnetic field lines are tangential to the Local Bubble surface and that this surface is defined by the model of Pelgrims et al. (2020), we test for a correlation between the measured dust polarization fraction and the angle the line of sight makes with the tangential magnetic field lines. However, we do not find evidence for this in sightlines where the dust extinction is dominated by the Local Bubble. We also do not find a correlation between the dust polarization fraction and the inclina-

tion angle between the Local Bubble wall defined by the model of O'Neill et al. (2024) and the plane of the sky. Therefore, we conclude that at least one of the commonly made assumptions must not hold. We hypothesize that dust structure beyond the Local Bubble wall plays a substantial role in determining the polarization structure of the dust emission. Our results show that simply projecting the Planck polarization data onto the Local Bubble geometry is not a well-motivated model for the magnetic field structure of the Local Bubble.

In Section 4, we test how dust complexity, i.e., how the 3D dust is distributed along the line of sight, affects the dust polarization fraction. We quantify the dust complexity for each sightline and group the sightlines into low- and high-complexity groups. We pair-match the sightlines across the two groups based on their column densities. For each pair, we subtract the dust polarization fraction of the sightline with low complexity from that of the sightline with high complexity. We find that on average, the dust polarization fraction of the sightlines with higher complexity is 2% lower than those with lower complexity. This is only true when considering dust out to 1.25 kpc. The result is not statistically different from null when considering dust out to 270 pc only. Note that our definition of complexity does not take into account the distance to different dust components. Future work could incorporate the effect of this distance into the analysis.

We test whether the order of magnitude of this result agrees with our expectation based on geometric depolarization. Padoan et al. (2001) model the polarized thermal dust emission from protostellar cores formed through supersonic turbulent flows within molecular clouds following the formalism in Fiege & Pudritz (2000). Fiege & Pudritz (2000) develops this formalism to model the submillimeter polarization patterns for filamentary molecular clouds. Fiege & Pudritz (2000) and Padoan et al. (2001) ignore the effects of self-absorption and scattering since this model is for submillimeter wavelengths at which the diffuse interstellar medium is optically thin. Padoan et al. (2001) further assume that the dust grain properties are constant and the temperature is uniform. Since these assumptions are valid for our order of magnitude estimation, we follow the same formalism here.

For this test, we consider sightlines with 2 clouds but different  $\mathcal{N}_c$  values. For simplicity, we assume each cloud to have a constant volume density, plane-of-sky magnetic field angle, and magnetic inclination angle along a certain sightline. Therefore, for a given sightline, we

write Equations 2, 3, and 4 as

$$I = \epsilon N_{\text{H}} - \frac{\alpha\epsilon}{2} \left( N_{\text{H},a} \cos^2 \gamma_a + N_{\text{H},b} \cos^2 \gamma_b - \frac{2}{3} N_{\text{H}} \right), \quad (12)$$

$$Q = -\alpha\epsilon (N_{\text{H},a} \cos 2\psi_a \cos^2 \gamma_a + N_{\text{H},b} \cos 2\psi_b \cos^2 \gamma_b), \quad (13)$$

$$U = -\alpha\epsilon (N_{\text{H},a} \sin 2\psi_a \cos^2 \gamma_a + N_{\text{H},b} \sin 2\psi_b \cos^2 \gamma_b), \quad (14)$$

where  $N_{\text{H},a}$  and  $N_{\text{H},b}$  are the column densities for each cloud,  $N_{\text{H}} = N_{\text{H},a} + N_{\text{H},b}$ ,  $\gamma_a$  and  $\gamma_b$  are the magnetic inclination angles of the two clouds, and  $\epsilon$  cancels out when calculating  $p$ .

We take  $N_{\text{H},a} > N_{\text{H},b}$ , i.e.,

$$\mathcal{N}_c = \frac{N_{\text{H},a} + N_{\text{H},b}}{N_{\text{H},a}}. \quad (15)$$

We divide Equations 12, 13, and 14 by  $N_{\text{H},a}$  to be able to write them in terms of  $\mathcal{N}_c$ . Therefore,

$$I/N_{\text{H},a} = \epsilon \mathcal{N}_c - \frac{\alpha\epsilon}{2} \left[ \cos^2 \gamma_a + (\mathcal{N}_c - 1) \cos^2 \gamma_b - \frac{2}{3} \mathcal{N}_c \right], \quad (16)$$

$$Q/N_{\text{H},a} = -\alpha\epsilon \left[ \cos 2\psi_a \cos^2 \gamma_a + (\mathcal{N}_c - 1) \cos 2\psi_b \cos^2 \gamma_b \right], \quad (17)$$

$$U/N_{\text{H},a} = -\alpha\epsilon \left[ \sin 2\psi_a \cos^2 \gamma_a + (\mathcal{N}_c - 1) \sin 2\psi_b \cos^2 \gamma_b \right], \quad (18)$$

where  $N_{\text{H},a}$  cancels out when calculating  $p$ .

We uniformly sample orientations in the range  $[0, \pi]$  for  $\psi_a$  and  $\psi_b$ , values in the range  $[0, 1]$  for  $\cos \gamma_a$  and  $\cos \gamma_b$ , and a value in the range  $[1, 1.1]$  for  $\mathcal{N}_c$  to calculate an instance of  $p(\mathcal{N}_c \leq 1.1)$ . We also sample different orientations and a value in the range  $[1.5, 2]$  for  $\mathcal{N}_c$  to calculate an instance of  $p(\mathcal{N}_c \geq 1.5)$ . We then subtract  $p(\mathcal{N}_c \leq 1.1)$  from  $p(\mathcal{N}_c \geq 1.5)$  as in Section 4. We repeat this 10,000 times and average the results. We set  $\alpha = 0.22$ , which corresponds to a maximum dust polarization fraction across the sky  $p_{\text{max}} = 0.22$ . This is the value Planck Collaboration et al. (2020a) observe for  $p_{\text{max}}$  at 353 GHz and 80' resolution. We get

$$\langle p(\mathcal{N}_c \geq 1.5) - p(\mathcal{N}_c \leq 1.1) \rangle = -0.013. \quad (19)$$

This mean difference depends on the value for  $\alpha$ . For instance, if we set  $\alpha = 0.15$  as in Padoan et al. (2001) instead, we get a mean difference of -0.009. However, our estimate for the mean difference agrees with the result we measure in Section 4 for all reasonable values of  $\alpha$ . Thus, our empirical result is consistent with our theoretical estimate for the dust depolarization attributable to the line-of-sight dust complexity.

Variations in the orientation of magnetic fields along the line of sight induce differences in the polarization angles of different dust components along the same sightline (Lee & Draine 1985; Tassis & Pavlidou 2015; King

et al. 2018). When the emission of those components has different spectral energy distributions (SEDs), a frequency-dependent variation of the observed dust polarization angle along that sightline emerges, a phenomenon known as line-of-sight frequency decorrelation. This decorrelation complicates the translation of polarized dust emission maps from one frequency to another. Current analysis within the BICEP/Keck field does not demonstrate evidence of this phenomenon (BICEP/Keck Collaboration et al. 2021, 2023). However, a statistically significant detection of line-of-sight frequency decorrelation has been identified in larger sky areas across sightlines intersecting multiple dust clouds with varying magnetic field orientations (Pelgrims et al. 2021). Since polarized dust emission is the major foreground for CMB polarization measurements at high frequencies, it is important to characterize how the spatial complexity of the magnetic field in the dust might affect the frequency dependence of the foreground signal. In this paper, we have presented evidence that the 3D spatial complexity of the dust affects the dust polarization signal, even at a fixed frequency.

The analysis in this paper highlights the importance of 3D dust mapping out to large distances. The dust distribution affects the dust polarization fraction, which has implications for the 3D magnetic field distribution. Since we expect higher complexity sightlines to have a lower dust polarization fraction on average, we would infer that the magnetic field is more uniform along a sightline if it has both a highly complex dust distribution and a large dust polarization fraction. This analysis was performed on the sightlines shown in Figure 6. Improvements to 3D dust modeling will allow us to look for this effect at the very high Galactic latitudes excluded here.

Given the significance of the 3D dust distribution on measurements of the polarized dust emission, these data can be combined with position-position-velocity maps of the neutral hydrogen-based dust polarization templates. These templates, constructed based on the orientation of neutral hydrogen filaments, have been shown to correlate very well with the measured dust polarization (Clark & Hensley 2019; Cukierman et al. 2023; BICEP/Keck Collaboration et al. 2023; Halal et al. 2024). Since the neutral hydrogen and dust trace similar volumes of the diffuse interstellar medium (Boulanger et al. 1996; Lenz et al. 2017), future work could morphologically match the position-position-position dust maps with the position-position-velocity neutral hydrogen-based maps to form 4D position-position-position-velocity maps of the magnetic field and polarized dust emission. Starlight polarization can also



be used to provide a tomographic view of the plane-of-the-sky magnetic field and polarized dust emission for sightlines with these measurements (Panopoulou et al. 2019; Tassis et al. 2018; Pelgrims et al. 2023, 2024). These data combined with Faraday tomography (Van Eck et al. 2017) or rotation measures (Tahani et al. 2018) can be used to constrain the 3D magnetic field structure.

We thank Gordian Edenhofer and Minjie Lei for insightful discussions. This work was supported by the National Science Foundation under grant No. AST-2106607. MT is supported by the Banting Fellowship (Natural Sciences and Engineering Research Council Canada) hosted at Stanford University and the Kavli Institute for Particle Astrophysics and Cosmology (KIPAC) Fellowship. This publication utilizes data from Planck, an ESA science mission funded by ESA Member States, NASA, and Canada. The computations in this paper were run on the Sherlock cluster, supported by the Stanford Research Computing Center at Stanford University.

*Software:* astropy (Astropy Collaboration et al. 2013, 2018), HEALPix<sup>3</sup> (Górski et al. 2005), healpy (Zonca et al. 2019), matplotlib (Hunter 2007), numpy (Oliphant 2015), scipy (Virtanen et al. 2020), dustmaps (Green 2018), astrodendro (Rosolowsky et al. 2008)

## APPENDIX

### A. ANALYSIS VARIATIONS

In this appendix, we list some of the results obtained from varying the main analysis choices in Section 4. These analysis variations are described and their results summarized in Section 4.6. In Table 1, we present some of the results obtained from varying the dendrogram parameters used in identifying the density peaks in the line-of-sight dust distribution and from varying the upper and lower thresholds in  $\mathcal{N}_c$  used for splitting the sightlines into low- and high-complexity groups. Table 2

lists the results of the same variations performed in Table 1 but when including the absolute value of the Galactic latitude as an additional confounding variable in the sightline matching across the two complexity groups. Finally, we present the results of sampling 1,000 sightlines from each of the two complexity groups with  $\mathcal{N}_c \leq 1.4$  and  $\mathcal{N}_c \leq 2.3$  before matching in Table 3. We find that the result in our main analysis is robust to all of these analysis variations.

## REFERENCES

- Alves, M. I. R., Boulanger, F., Ferrière, K., & Montier, L. 2018, A&A, 611, L5, doi: [10.1051/0004-6361/201832637](https://doi.org/10.1051/0004-6361/201832637)
- Anders, F., Khalatyan, A., Chiappini, C., et al. 2019, A&A, 628, A94, doi: [10.1051/0004-6361/201935765](https://doi.org/10.1051/0004-6361/201935765)
- Andersson, B. G., Lazarian, A., & Vaillancourt, J. E. 2015, ARA&A, 53, 501, doi: [10.1146/annurev-astro-082214-122414](https://doi.org/10.1146/annurev-astro-082214-122414)
- Andersson, B. G., & Potter, S. B. 2006, ApJL, 640, L51, doi: [10.1086/503199](https://doi.org/10.1086/503199)
- Astropy Collaboration, Robitaille, T. P., Tollerud, E. J., et al. 2013, A&A, 558, A33, doi: [10.1051/0004-6361/201322068](https://doi.org/10.1051/0004-6361/201322068)
- Astropy Collaboration, Price-Whelan, A. M., Sipőcz, B. M., et al. 2018, AJ, 156, 123, doi: [10.3847/1538-3881/aabc4f](https://doi.org/10.3847/1538-3881/aabc4f)
- Barnes, A. T., Watkins, E. J., Meidt, S. E., et al. 2023, ApJL, 944, L22, doi: [10.3847/2041-8213/aca7b9](https://doi.org/10.3847/2041-8213/aca7b9)
- Berdyugin, A., Piirola, V., & Teerikorpi, P. 2014, A&A, 561, A24, doi: [10.1051/0004-6361/201322604](https://doi.org/10.1051/0004-6361/201322604)
- Bialy, S., Zucker, C., Goodman, A., et al. 2021, ApJL, 919, L5, doi: [10.3847/2041-8213/ac1ff95](https://doi.org/10.3847/2041-8213/ac1ff95)

<sup>3</sup> <http://healpix.sourceforge.net/>

$\Delta_n$	$\#_{\text{voxels}}$	low complexity	high complexity	# of matched pairs	$\mu_{\Delta p_{353}}$	$\sigma_{\Delta p_{353}}$	p-value
<b><math>7 \times 10^{-6}</math></b>	<b>3</b>	<b><math>\mathcal{N}_c \leq 1.1</math></b>	<b><math>\mathcal{N}_c \geq 1.5</math></b>	<b>753</b>	<b><math>-1.47 \times 10^{-2}</math></b>	<b><math>0.22 \times 10^{-2}</math></b>	<b>&lt; 0.001</b>
$7 \times 10^{-6}$	3	$\mathcal{N}_c \leq 1.4$	$\mathcal{N}_c \geq 2.3$	4,674	$-1.10 \times 10^{-2}$	$0.08 \times 10^{-2}$	< 0.001
$9 \times 10^{-6}$	3	$\mathcal{N}_c \leq 1.1$	$\mathcal{N}_c \geq 1.5$	776	$-1.33 \times 10^{-2}$	$0.26 \times 10^{-2}$	< 0.001
$9 \times 10^{-6}$	3	$\mathcal{N}_c \leq 1.4$	$\mathcal{N}_c \geq 2.3$	4,719	$-1.01 \times 10^{-2}$	$0.12 \times 10^{-2}$	< 0.001
$5 \times 10^{-6}$	5	$\mathcal{N}_c \leq 1.1$	$\mathcal{N}_c \geq 1.5$	1,005	$-0.98 \times 10^{-2}$	$0.20 \times 10^{-2}$	< 0.001
$5 \times 10^{-6}$	5	$\mathcal{N}_c \leq 1.4$	$\mathcal{N}_c \geq 2.3$	5,311	$-0.82 \times 10^{-2}$	$0.14 \times 10^{-2}$	< 0.001
$3 \times 10^{-6}$	5	$\mathcal{N}_c \leq 1.1$	$\mathcal{N}_c \geq 1.5$	984	$-1.00 \times 10^{-2}$	$0.21 \times 10^{-2}$	< 0.001
$3 \times 10^{-6}$	5	$\mathcal{N}_c \leq 1.4$	$\mathcal{N}_c \geq 2.3$	5,284	$-0.80 \times 10^{-2}$	$0.13 \times 10^{-2}$	< 0.001

**Table 1.** Results obtained from varying both the dendrogram parameters ( $\Delta_n$  and  $\#_{\text{voxels}}$ ) used to identify the density peaks in the line-of-sight dust distribution and from varying the upper and lower thresholds in  $\mathcal{N}_c$  used to divide the sightlines into low- and high-complexity groups. The results of the main analysis are bolded in the first row. The mean and standard deviation in the  $\mu_{\Delta p_{353}}$  and  $\sigma_{\Delta p_{353}}$  columns are over the 12 posterior samples of the Edenhofer et al. (2023) maps.

$\Delta_n$	$\#_{\text{voxels}}$	low complexity	high complexity	# of matched pairs	$\mu_{\Delta p_{353}}$	$\sigma_{\Delta p_{353}}$	p-value
$7 \times 10^{-6}$	3	$\mathcal{N}_c \leq 1.1$	$\mathcal{N}_c \geq 1.5$	753	$-1.45 \times 10^{-2}$	$0.23 \times 10^{-2}$	< 0.001
$7 \times 10^{-6}$	3	$\mathcal{N}_c \leq 1.4$	$\mathcal{N}_c \geq 2.3$	4,674	$-1.02 \times 10^{-2}$	$0.08 \times 10^{-2}$	< 0.001
$9 \times 10^{-6}$	3	$\mathcal{N}_c \leq 1.1$	$\mathcal{N}_c \geq 1.5$	776	$-1.31 \times 10^{-2}$	$0.34 \times 10^{-2}$	< 0.001
$9 \times 10^{-6}$	3	$\mathcal{N}_c \leq 1.4$	$\mathcal{N}_c \geq 2.3$	4,719	$-1.00 \times 10^{-2}$	$0.15 \times 10^{-2}$	< 0.001
$5 \times 10^{-6}$	5	$\mathcal{N}_c \leq 1.1$	$\mathcal{N}_c \geq 1.5$	1,005	$-0.60 \times 10^{-2}$	$0.17 \times 10^{-2}$	< 0.001
$5 \times 10^{-6}$	5	$\mathcal{N}_c \leq 1.4$	$\mathcal{N}_c \geq 2.3$	5,311	$-0.82 \times 10^{-2}$	$0.13 \times 10^{-2}$	< 0.001
$3 \times 10^{-6}$	5	$\mathcal{N}_c \leq 1.1$	$\mathcal{N}_c \geq 1.5$	984	$-0.67 \times 10^{-2}$	$0.22 \times 10^{-2}$	< 0.001
$3 \times 10^{-6}$	5	$\mathcal{N}_c \leq 1.4$	$\mathcal{N}_c \geq 2.3$	5,284	$-0.80 \times 10^{-2}$	$0.13 \times 10^{-2}$	< 0.001

**Table 2.** Results obtained from the same variations described in Table 1, where the sightline matching over the two complexity groups in this case includes the absolute value of the Galactic latitude as an additional confounding variable. The mean and standard deviation in the  $\mu_{\Delta p_{353}}$  and  $\sigma_{\Delta p_{353}}$  columns are over the 12 posterior samples of the Edenhofer et al. (2023) maps.

$\Delta_n$	$\#_{\text{voxels}}$	$\mu_{\Delta p_{353}}$	$\sigma_{\Delta p_{353}}$	p-value
$7 \times 10^{-6}$	3	$-1.08 \times 10^{-2}$	$0.17 \times 10^{-2}$	< 0.001
$9 \times 10^{-6}$	3	$-1.14 \times 10^{-2}$	$0.24 \times 10^{-2}$	< 0.001
$5 \times 10^{-6}$	5	$-0.84 \times 10^{-2}$	$0.17 \times 10^{-2}$	< 0.001
$3 \times 10^{-6}$	5	$-0.89 \times 10^{-2}$	$0.18 \times 10^{-2}$	< 0.001

**Table 3.** Results obtained from sampling 1,000 sightlines from each of the  $\mathcal{N}_c \leq 1.4$  and  $\mathcal{N}_c \geq 2.3$  complexity groups before matching. The different rows are for different variations in the dendrogram parameters ( $\Delta_n$  and  $\#_{\text{voxels}}$ ) used in identifying the density peaks in the line-of-sight dust distribution. The mean and standard deviation in the  $\mu_{\Delta p_{353}}$  and  $\sigma_{\Delta p_{353}}$  columns are over the 12 posterior samples of the Edenhofer et al. (2023) maps.

BICEP/Keck Collaboration, Ade, P. A. R., Ahmed, Z., et al. 2021, PhRvL, 127, 151301,

doi: [10.1103/PhysRevLett.127.151301](https://doi.org/10.1103/PhysRevLett.127.151301)

—. 2023, ApJ, 945, 72, doi: [10.3847/1538-4357/acb64c](https://doi.org/10.3847/1538-4357/acb64c)

Boulanger, F., Abergel, A., Bernard, J. P., et al. 1996, A&A, 312, 256

Breitschwerdt, D., Feige, J., Schulreich, M. M., et al. 2016, Nature, 532, 73, doi: [10.1038/nature17424](https://doi.org/10.1038/nature17424)

Cahlon, S., Zucker, C., Goodman, A., Lada, C., & Alves, J. 2023, arXiv e-prints, arXiv:2308.14794,

doi: [10.48550/arXiv.2308.14794](https://doi.org/10.48550/arXiv.2308.14794)

Chen, C.-Y., King, P. K., Li, Z.-Y., Fissel, L. M., & Mazzei, R. R. 2019, MNRAS, 485, 3499,

doi: [10.1093/mnras/stz618](https://doi.org/10.1093/mnras/stz618)

Clark, S. E. 2018, ApJL, 857, L10,

doi: [10.3847/2041-8213/aabb54](https://doi.org/10.3847/2041-8213/aabb54)

Clark, S. E., & Hensley, B. S. 2019, ApJ, 887, 136,

doi: [10.3847/1538-4357/ab5803](https://doi.org/10.3847/1538-4357/ab5803)

Clark, S. E., Peek, J. E. G., & Putman, M. E. 2014, ApJ, 789, 82, doi: [10.1088/0004-637X/789/1/82](https://doi.org/10.1088/0004-637X/789/1/82)

Cotton, D. V., Marshall, J. P., Frisch, P. C., et al. 2019, MNRAS, 483, 3636, doi: [10.1093/mnras/sty3318](https://doi.org/10.1093/mnras/sty3318)

Cox, D. P., & Reynolds, R. J. 1987, ARA&A, 25, 303, doi: [10.1146/annurev.aa.25.090187.001511](https://doi.org/10.1146/annurev.aa.25.090187.001511)

Cukierman, A. J., Clark, S. E., & Halal, G. 2023, ApJ, 946, 106, doi: [10.3847/1538-4357/acb0c4](https://doi.org/10.3847/1538-4357/acb0c4)

Cutri, R. M., Wright, E. L., Conrow, T., et al. 2013, Explanatory Supplement to the AllWISE Data Release Products, Explanatory Supplement to the AllWISE Data Release Products, by R. M. Cutri et al.

- Dawson, J. R. 2013, *PASA*, 30, e025, doi: [10.1017/pas.2013.002](https://doi.org/10.1017/pas.2013.002)
- Edenhofer, G., Zucker, C., Frank, P., et al. 2023, arXiv e-prints, arXiv:2308.01295, doi: [10.48550/arXiv.2308.01295](https://doi.org/10.48550/arXiv.2308.01295)
- Elmegreen, B. G. 2011, in *EAS Publications Series*, Vol. 51, *EAS Publications Series*, ed. C. Charbonnel & T. Montmerle, 45–58, doi: [10.1051/eas/1151004](https://doi.org/10.1051/eas/1151004)
- Enßlin, T. A. 2019, *Annalen der Physik*, 531, 1800127, doi: [10.1002/andp.201800127](https://doi.org/10.1002/andp.201800127)
- Farhang, A., van Loon, J. T., Khosroshahi, H. G., Javadi, A., & Bailey, M. 2019, *Nature Astronomy*, 3, 922, doi: [10.1038/s41550-019-0814-z](https://doi.org/10.1038/s41550-019-0814-z)
- Ferrière, K. M. 2001, *Reviews of Modern Physics*, 73, 1031, doi: [10.1103/RevModPhys.73.1031](https://doi.org/10.1103/RevModPhys.73.1031)
- Fiege, J. D., & Pudritz, R. E. 2000, *ApJ*, 544, 830, doi: [10.1086/317228](https://doi.org/10.1086/317228)
- Finkbeiner, D. P. 2003, *ApJS*, 146, 407, doi: [10.1086/374411](https://doi.org/10.1086/374411)
- Fitzpatrick, E. L., Massa, D., Gordon, K. D., Bohlin, R., & Clayton, G. C. 2019, *ApJ*, 886, 108, doi: [10.3847/1538-4357/ab4c3a](https://doi.org/10.3847/1538-4357/ab4c3a)
- Flewelling, H. A., Magnier, E. A., Chambers, K. C., et al. 2020, *ApJS*, 251, 7, doi: [10.3847/1538-4365/abb82d](https://doi.org/10.3847/1538-4365/abb82d)
- Frisch, P. C., Andersson, B. G., Berdyugin, A., et al. 2012, *ApJ*, 760, 106, doi: [10.1088/0004-637X/760/2/106](https://doi.org/10.1088/0004-637X/760/2/106)
- Frisch, P. C., Berdyugin, A., Pirola, V., et al. 2015, *ApJ*, 814, 112, doi: [10.1088/0004-637X/814/2/112](https://doi.org/10.1088/0004-637X/814/2/112)
- Gaia Collaboration, Brown, A. G. A., Vallenari, A., et al. 2018, *A&A*, 616, A1, doi: [10.1051/0004-6361/201833051](https://doi.org/10.1051/0004-6361/201833051)
- Gaia Collaboration, Vallenari, A., Brown, A. G. A., et al. 2023, *A&A*, 674, A1, doi: [10.1051/0004-6361/202243940](https://doi.org/10.1051/0004-6361/202243940)
- Gontcharov, G. A., & Mosenkov, A. V. 2019, *MNRAS*, 483, 299, doi: [10.1093/mnras/sty2978](https://doi.org/10.1093/mnras/sty2978)
- Górski, K. M., Hivon, E., Banday, A. J., et al. 2005, *ApJ*, 622, 759, doi: [10.1086/427976](https://doi.org/10.1086/427976)
- Green, G. M. 2018, *Journal of Open Source Software*, 3, 695, doi: [10.21105/joss.00695](https://doi.org/10.21105/joss.00695)
- Halal, G., Clark, S. E., Cukierman, A., Beck, D., & Kuo, C.-L. 2024, *ApJ*, 961, 29, doi: [10.3847/1538-4357/ad06aa](https://doi.org/10.3847/1538-4357/ad06aa)
- Halal, G., Clark, S. E., & Tahani, M. 2024, *Halal et al. 2024 3D Dust Complexity Maps, V1*, Harvard Dataverse, doi: [10.7910/DVN/IW09AE](https://doi.org/10.7910/DVN/IW09AE)
- Heiles, C. 1984, *ApJS*, 55, 585, doi: [10.1086/190970](https://doi.org/10.1086/190970)
- . 1997, *ApJS*, 111, 245, doi: [10.1086/313010](https://doi.org/10.1086/313010)
- Heiles, C., & Haverkorn, M. 2012, *SSRv*, 166, 293, doi: [10.1007/s11214-012-9866-4](https://doi.org/10.1007/s11214-012-9866-4)
- Hensley, B. S., Zhang, C., & Bock, J. J. 2019, *ApJ*, 887, 159, doi: [10.3847/1538-4357/ab5183](https://doi.org/10.3847/1538-4357/ab5183)
- Hunter, J. D. 2007, *Computing in Science and Engineering*, 9, 90, doi: [10.1109/MCSE.2007.55](https://doi.org/10.1109/MCSE.2007.55)
- Hutschenreuter, S., Haverkorn, M., Frank, P., Raycheva, N. C., & Enßlin, T. A. 2023, arXiv e-prints, arXiv:2304.12350, doi: [10.48550/arXiv.2304.12350](https://doi.org/10.48550/arXiv.2304.12350)
- Inutsuka, S.-i., Inoue, T., Iwasaki, K., & Hosokawa, T. 2015, *A&A*, 580, A49, doi: [10.1051/0004-6361/201425584](https://doi.org/10.1051/0004-6361/201425584)
- Kim, C.-G., & Ostriker, E. C. 2015, *ApJ*, 802, 99, doi: [10.1088/0004-637X/802/2/99](https://doi.org/10.1088/0004-637X/802/2/99)
- King, P. K., Chen, C.-Y., Fissel, L. M., & Li, Z.-Y. 2019, *MNRAS*, 490, 2760, doi: [10.1093/mnras/stz2628](https://doi.org/10.1093/mnras/stz2628)
- King, P. K., Fissel, L. M., Chen, C.-Y., & Li, Z.-Y. 2018, *MNRAS*, 474, 5122, doi: [10.1093/mnras/stx3096](https://doi.org/10.1093/mnras/stx3096)
- Kothes, R., & Brown, J.-A. 2009, in *Cosmic Magnetic Fields: From Planets, to Stars and Galaxies*, ed. K. G. Strassmeier, A. G. Kosovichev, & J. E. Beckman, Vol. 259, 75–80, doi: [10.1017/S1743921309030087](https://doi.org/10.1017/S1743921309030087)
- Krumholz, M. R., Stone, J. M., & Gardiner, T. A. 2007, *ApJ*, 671, 518, doi: [10.1086/522665](https://doi.org/10.1086/522665)
- Lallement, R., Babusiaux, C., Vergely, J. L., et al. 2019, *A&A*, 625, A135, doi: [10.1051/0004-6361/201834695](https://doi.org/10.1051/0004-6361/201834695)
- Lallement, R., Vergely, J. L., Valette, B., et al. 2014, *A&A*, 561, A91, doi: [10.1051/0004-6361/201322032](https://doi.org/10.1051/0004-6361/201322032)
- Lallement, R., Welsh, B. Y., Vergely, J. L., Crifo, F., & Sfeir, D. 2003, *A&A*, 411, 447, doi: [10.1051/0004-6361:20031214](https://doi.org/10.1051/0004-6361:20031214)
- Lee, H. M., & Draine, B. T. 1985, *ApJ*, 290, 211, doi: [10.1086/162974](https://doi.org/10.1086/162974)
- Lei, M., & Clark, S. E. 2023, arXiv e-prints, arXiv:2312.03846, doi: [10.48550/arXiv.2312.03846](https://doi.org/10.48550/arXiv.2312.03846)
- Leike, R. H., Glatzle, M., & Enßlin, T. A. 2020, *A&A*, 639, A138, doi: [10.1051/0004-6361/202038169](https://doi.org/10.1051/0004-6361/202038169)
- Lenz, D., Hensley, B. S., & Doré, O. 2017, *ApJ*, 846, 38, doi: [10.3847/1538-4357/aa84af](https://doi.org/10.3847/1538-4357/aa84af)
- Leroy, J. L. 1999, *A&A*, 346, 955
- Liu, W., Chiao, M., Collier, M. R., et al. 2017, *ApJ*, 834, 33, doi: [10.3847/1538-4357/834/1/33](https://doi.org/10.3847/1538-4357/834/1/33)
- Maconi, E., Soler, J. D., Reissl, S., et al. 2023, *MNRAS*, 523, 5995, doi: [10.1093/mnras/stad1854](https://doi.org/10.1093/mnras/stad1854)
- Maíz-Apellániz, J. 2001, *ApJL*, 560, L83, doi: [10.1086/324016](https://doi.org/10.1086/324016)
- Manchester, R. N., Hobbs, G. B., Teoh, A., & Hobbs, M. 2005, *AJ*, 129, 1993, doi: [10.1086/428488](https://doi.org/10.1086/428488)
- Marchal, A., & Martin, P. G. 2023, *ApJ*, 942, 70, doi: [10.3847/1538-4357/aca4d2](https://doi.org/10.3847/1538-4357/aca4d2)
- Medan, I., & Andersson, B. G. 2019, *ApJ*, 873, 87, doi: [10.3847/1538-4357/ab063c](https://doi.org/10.3847/1538-4357/ab063c)
- Oliphant, T. E. 2015, *Guide to NumPy*, 2nd edn. (North Charleston, SC, USA: CreateSpace Independent Publishing Platform)

- O'Neill, T. J., Zucker, C., Goodman, A. A., & Edenhofer, G. 2024, arXiv e-prints, arXiv:2403.04961, doi: [10.48550/arXiv.2403.04961](https://doi.org/10.48550/arXiv.2403.04961)
- O'Neill, T., Goodman, A., Soler, J., Han, J. J., & Zucker, C. 2023, doi: [10.22541/au.167303779.92162611/v3](https://doi.org/10.22541/au.167303779.92162611/v3)
- Padoan, P., Goodman, A., Draine, B. T., et al. 2001, ApJ, 559, 1005, doi: [10.1086/322504](https://doi.org/10.1086/322504)
- Panopoulou, G. V., & Lenz, D. 2020, ApJ, 902, 120, doi: [10.3847/1538-4357/abb6f5](https://doi.org/10.3847/1538-4357/abb6f5)
- Panopoulou, G. V., Tassis, K., Skalidis, R., et al. 2019, ApJ, 872, 56, doi: [10.3847/1538-4357/aafdb2](https://doi.org/10.3847/1538-4357/aafdb2)
- Pattle, K., Fissel, L., Tahani, M., Liu, T., & Ntormousi, E. 2023, in *Astronomical Society of the Pacific Conference Series*, Vol. 534, *Protostars and Planets VII*, ed. S. Inutsuka, Y. Aikawa, T. Muto, K. Tomida, & M. Tamura, 193, doi: [10.48550/arXiv.2203.11179](https://doi.org/10.48550/arXiv.2203.11179)
- Pelgrims, V., Clark, S. E., Hensley, B. S., et al. 2021, A&A, 647, A16, doi: [10.1051/0004-6361/202040218](https://doi.org/10.1051/0004-6361/202040218)
- Pelgrims, V., Ferrière, K., Boulanger, F., Lallement, R., & Montier, L. 2020, A&A, 636, A17, doi: [10.1051/0004-6361/201937157](https://doi.org/10.1051/0004-6361/201937157)
- Pelgrims, V., Panopoulou, G. V., Tassis, K., et al. 2023, A&A, 670, A164, doi: [10.1051/0004-6361/202244625](https://doi.org/10.1051/0004-6361/202244625)
- Pelgrims, V., Mandarakas, N., Skalidis, R., et al. 2024, arXiv e-prints, arXiv:2404.10821, doi: [10.48550/arXiv.2404.10821](https://doi.org/10.48550/arXiv.2404.10821)
- Pelkonen, V. M., Juvela, M., & Padoan, P. 2007, A&A, 461, 551, doi: [10.1051/0004-6361:20065838](https://doi.org/10.1051/0004-6361:20065838)
- Planck Collaboration, Abergel, A., Ade, P. A. R., et al. 2014, A&A, 571, A11, doi: [10.1051/0004-6361/201323195](https://doi.org/10.1051/0004-6361/201323195)
- Planck Collaboration, Aghanim, N., Ashdown, M., et al. 2016a, A&A, 596, A109, doi: [10.1051/0004-6361/201629022](https://doi.org/10.1051/0004-6361/201629022)
- Planck Collaboration, Adam, R., Ade, P. A. R., et al. 2016b, A&A, 594, A10, doi: [10.1051/0004-6361/201525967](https://doi.org/10.1051/0004-6361/201525967)
- Planck Collaboration, Aghanim, N., Akrami, Y., et al. 2020a, A&A, 641, A12, doi: [10.1051/0004-6361/201833885](https://doi.org/10.1051/0004-6361/201833885)
- . 2020b, A&A, 641, A1, doi: [10.1051/0004-6361/201833880](https://doi.org/10.1051/0004-6361/201833880)
- Plaszczynski, S., Montier, L., Levrier, F., & Tristram, M. 2014, MNRAS, 439, 4048, doi: [10.1093/mnras/stu270](https://doi.org/10.1093/mnras/stu270)
- Purcell, E. M. 1975, in *The Dusty Universe*, ed. G. B. Field & A. G. W. Cameron, 155–167
- Puspitarini, L., & Lallement, R. 2012, A&A, 545, A21, doi: [10.1051/0004-6361/201219284](https://doi.org/10.1051/0004-6361/201219284)
- Remazeilles, M., Delabrouille, J., & Cardoso, J.-F. 2011, MNRAS, 418, 467, doi: [10.1111/j.1365-2966.2011.19497.x](https://doi.org/10.1111/j.1365-2966.2011.19497.x)
- Rosolowsky, E. W., Pineda, J. E., Kauffmann, J., & Goodman, A. A. 2008, ApJ, 679, 1338, doi: [10.1086/587685](https://doi.org/10.1086/587685)
- Sandstrom, K. M., Koch, E. W., Leroy, A. K., et al. 2023, ApJL, 944, L8, doi: [10.3847/2041-8213/aca972](https://doi.org/10.3847/2041-8213/aca972)
- Santos, F. P., Corradi, W., & Reis, W. 2011, ApJ, 728, 104, doi: [10.1088/0004-637X/728/2/104](https://doi.org/10.1088/0004-637X/728/2/104)
- Schulreich, M. M., Feige, J., & Breitschwerdt, D. 2023, A&A, 680, A39, doi: [10.1051/0004-6361/202347532](https://doi.org/10.1051/0004-6361/202347532)
- Sfeir, D. M., Lallement, R., Crifo, F., & Welsh, B. Y. 1999, A&A, 346, 785
- Skalidis, R., & Pelgrims, V. 2019, A&A, 631, L11, doi: [10.1051/0004-6361/201936547](https://doi.org/10.1051/0004-6361/201936547)
- Skrutskie, M. F., Cutri, R. M., Stiening, R., et al. 2006, AJ, 131, 1163, doi: [10.1086/498708](https://doi.org/10.1086/498708)
- Soler, J. D., Bracco, A., & Pon, A. 2018, A&A, 609, L3, doi: [10.1051/0004-6361/201732203](https://doi.org/10.1051/0004-6361/201732203)
- Sullivan, C. H., Fissel, L. M., King, P. K., et al. 2021, MNRAS, 503, 5006, doi: [10.1093/mnras/stab596](https://doi.org/10.1093/mnras/stab596)
- Tahani, M., Plume, R., Brown, J. C., & Kainulainen, J. 2018, A&A, 614, A100, doi: [10.1051/0004-6361/201732219](https://doi.org/10.1051/0004-6361/201732219)
- Tahani, M., Glover, J., Lupypciw, W., et al. 2022a, A&A, 660, L7, doi: [10.1051/0004-6361/202243322](https://doi.org/10.1051/0004-6361/202243322)
- Tahani, M., Lupypciw, W., Glover, J., et al. 2022b, A&A, 660, A97, doi: [10.1051/0004-6361/202141170](https://doi.org/10.1051/0004-6361/202141170)
- Tahani, M., Bastien, P., Furuya, R. S., et al. 2023, ApJ, 944, 139, doi: [10.3847/1538-4357/acac81](https://doi.org/10.3847/1538-4357/acac81)
- Tassis, K., & Pavlidou, V. 2015, MNRAS, 451, L90, doi: [10.1093/mnrasl/slv077](https://doi.org/10.1093/mnrasl/slv077)
- Tassis, K., Ramaprakash, A. N., Readhead, A. C. S., et al. 2018, arXiv e-prints, arXiv:1810.05652, doi: [10.48550/arXiv.1810.05652](https://doi.org/10.48550/arXiv.1810.05652)
- Van Eck, C. L., Haverkorn, M., Alves, M. I. R., et al. 2017, A&A, 597, A98, doi: [10.1051/0004-6361/201629707](https://doi.org/10.1051/0004-6361/201629707)
- Van Eck, C. L., Gaensler, B. M., Hutschenreuter, S., et al. 2023, ApJS, 267, 28, doi: [10.3847/1538-4365/acda24](https://doi.org/10.3847/1538-4365/acda24)
- Vergely, J. L., Lallement, R., & Cox, N. L. J. 2022, A&A, 664, A174, doi: [10.1051/0004-6361/202243319](https://doi.org/10.1051/0004-6361/202243319)
- Virtanen, P., Gommers, R., Oliphant, T. E., et al. 2020, *Nature Methods*, 17, 261, doi: [10.1038/s41592-019-0686-2](https://doi.org/10.1038/s41592-019-0686-2)
- Watkins, E. J., Barnes, A. T., Henny, K., et al. 2023, ApJL, 944, L24, doi: [10.3847/2041-8213/aca6e4](https://doi.org/10.3847/2041-8213/aca6e4)
- Welsh, B. Y. 1991, ApJ, 373, 556, doi: [10.1086/170074](https://doi.org/10.1086/170074)
- Welsh, B. Y., Sallmen, S., & Lallement, R. 2004, A&A, 414, 261, doi: [10.1051/0004-6361:20034367](https://doi.org/10.1051/0004-6361:20034367)
- West, J. L., Safi-Harb, S., Jaffe, T., et al. 2016, A&A, 587, A148, doi: [10.1051/0004-6361/201527001](https://doi.org/10.1051/0004-6361/201527001)
- Zhang, X., Green, G. M., & Rix, H.-W. 2023, MNRAS, 524, 1855, doi: [10.1093/mnras/stad1941](https://doi.org/10.1093/mnras/stad1941)

Zonca, A., Singer, L., Lenz, D., et al. 2019, The Journal of Open Source Software, 4, 1298, doi: [10.21105/joss.01298](https://doi.org/10.21105/joss.01298)  
Zucker, C., Goodman, A., Alves, J., et al. 2021, ApJ, 919, 35, doi: [10.3847/1538-4357/ac1f96](https://doi.org/10.3847/1538-4357/ac1f96)

Zucker, C., Goodman, A. A., Alves, J., et al. 2022, Nature, 601, 334, doi: [10.1038/s41586-021-04286-5](https://doi.org/10.1038/s41586-021-04286-5)